UNIVERSITY OF KUOPIO, Faculty of Natural and Environmental Sciences
Physics
Medical Physics
Kervinen Mikko Tapio: Attenuation and Collimator Modeling in Limited-Projection Emission Tomography with Application to Dose Calculation in Radionuclide Therapy
Master of Science thesis, 65 pages.
Supervisors:
Ph.D. Pasi Karjalainen
Ph.D. Tapani Lahtinen
M.Sc. Aku Seppänen
12th September 2001

Keywords: Single Photon Emission Computed Tomography (SPECT), Targeted Radionuclide Therapy (TRT), collimator correction, attenuation, Region Of Interest (ROI), maximum likelihood estimation, inverse problem, dose calculation

Radionuclide therapy is an increasingly important technique in cancer treatment. The most common application of radionuclide therapy is the treatment of hyperthyroidism and thyroid cancer with ^{131}I. In order to evaluate the efficiency of the treatment, accurate dose calculations are needed.

Accurate dose calculation in radionuclide therapy requires on-therapy imaging of the activity distribution in target organ. When the activity distribution is determined and the attenuation distribution in the target is known -at least approximately- the computation of the dose of the target is straightforward. On-therapy imaging of the activity can not be performed using standard clinical SPECT due to the high count rates and high photon energies of the therapeutic compounds. 6P-SPECT is a novel application for on-therapy imaging of radionuclide therapy. In 6P-SPECT heavy one-row collimator system is used for acquiring six simultaneous projections of the activity distribution. The activity distribution is then reconstructed based on measured projections.

Due to the low number of projections in 6P-SPECT the traditional tomographic reconstruction methods are insufficient and the image reconstruction requires accurate modeling of the imaging system, as well as modern reconstruction methods. In this thesis we consider three-dimensional modeling of the collimator response and inhomogeneous attenuation. However, scattering effects are ignored.

The statistical nature of radiation is taken into account in reconstruction by using maximum likelihood estimate. The used maximum likelihood expectation maximization (ML-EM) algorithm produces superior estimates compared to the classical filtered back projection and least squares estimates.

In addition to the reconstruction of the activity we consider the dose calculation based on the reconstructions. In the dose calculation we take into account the attenuation of the non-water-equivalent structures by using the effective attenuation coefficient technique. The calculated dose distribution can be calibrated by a single surface dose measurement.

We built two phantoms in order to evaluate the computational methods with real data. The reconstruction of activity distribution was then tested with a circular water phantom. Plastic phantom was used to measure both projections of activity distribution and dose profiles inside the phantom.

This thesis is available on http://www.venda.uku.fi/∼kervinen/thesis.html

Acknowledgments

This study was carried out in the Department of Applied Physics at the University of Kuopio during 2000-2001. I thank my supervisors Pasi Karjalainen, Ph.D. for the guidance and support during this work, Tapani Lahtinen, Ph.D. for providing the materials and clinical point of view and Aku Seppänen, M.Sc. for answering to the numerous questions related to this work.

I also thank the official reviewer Samuli Siltanen Ph.D.

I also want to thank my parents Erja and Jouko Kervinen for their encouragement and support during my studies.

Finally I express my gratitude for Liina and Gipsy for their constant support.

Kuopio, August 2001.

Mikko Kervinen

Abbreviations

6P-SPECT	Single Photon Emission Computed Tomography from six Projections
CT	Computed Tomography
FBP	Filtered Back Projection
FFT	Fast Fourier Transform or Finite Fourier Transform
FWHM	Full Width Half Maximum
IFFT	Inverse Fast Fourier Transform or Inverse Finite Fourier Transform
LS	Least Squares
MAP	Maximum a Posteriori
MIRD	Medical Internal Radiation Dose
ML	Maximum Likelihood
MN	Minimum Norm
PET	Positron Emission Tomography
ROI	Region of Interest
SDCC	Surface Dose Correction Coefficient
SPECT	Single Photon Emission Computed Tomography
TLD	Thermoluminescence Dosiometry
TRT	Targeted Radionuclide Therapy
ZP	Zero Padding

Contents

Chapter 1

Introduction

In this section we consider the basics of radionuclide treatment and radioisotope imaging. Furthermore, the use of radioisotope imaging in validation of radionuclide therapy is discussed. Radionuclide therapy is a method of cancer treatment, where a large amount of radioactive compound is injected or administered orally in to the patient. The applied compound has metabolic properties that make the accumulation of the compound easier in the target tissues or organs. As in external beam therapy the tumor tissue is destroyed by the radiation effects. Since the absorbed dose in the target tissue is critical for the efficiency of the treatment, dose measurements are required. Usually therapy planning is made by exposing the patient with lower activity of the same compound and imaging the activity distribution with gamma-camera. If the distribution of the compound is suitable for treatment, higher activity of therapeutic compound is administered. The on-therapy imaging of radionuclide treatments is difficult since the clinical gamma-cameras are not designed to image high activities and high photon energies associated with radionuclide treatments.

Of the methods of radioisotope imaging we make a special emphasis on Single Photon Emission Computed Tomography (SPECT). SPECT is an imaging modality where the three-dimensional activity distribution inside the patient can be reconstructed using several planar images acquired with a gamma-camera. There are several approaches to image the on-therapy distribution during radionuclide treatment with clinical gamma-cameras. The main problems are insufficient collimation and high count rates that saturate the electronics of the camera. Despite the problems, SPECT gives more accurate quantitative results of the activity distribution than other methods that are based on only planar imaging. In this section -and in the whole thesis- we concentrate especially on 6P-SPECT, a simple collimation system designed for on-therapy imaging with high activities and especially with thyroid treatments [28].

1.1 Targeted radionuclide therapy

1.1.1 Basics

Radionuclide therapy is an increasingly important technique in cancer treatment. The main goal in this technique is to get the concentration of the radiopharmaceutical high in target tissue and to keep the concentration low in the rest of the body. This is achieved by using the so called tumor-seeking compounds. When the activity in the tumor is high the tumor-tissue will be destroyed efficiently. The tracer molecules are selected to have chemical properties that make stable labeling possible. Also the metabolism and kinetics must match the properties of the radioactive label. Specific metabolic characteristics and biological properties of the tumors are exploited for diagnosis and follow up with diagnostic compounds. Same information can also be applied for targeting the therapeutic nuclides into tumors. The most important property of the radiopharmaceutical is the specificity to accumulate in the target tissue. When the localization of the radiopharmaceutical is accurate enough, the technique is called Targeted Radionuclide Therapy (TRT) [28]. It has also been shown that patients treated with radionuclide therapy have smaller risk of leukaemia and second cancers than the patients treated with chemotherapy and external-beam radiotherapy [17].

Another way to get the activity to the tumor is to use sealed sources that are placed in the tumor tissue surgically or through the skin. This method is applied for example in the case of prostate cancer (prostate seed therapy with ^{125}I). In seed therapy the localization of the sources is accurate and dose can be limited in a small area. Also other isotopes have been applied in seed therapy, for example ^{192}Ir and ^{103}Pd.

Targeted radionuclide therapy has been used in several different treatments. One is the ^{131}I therapy for thyroid carcinoma and thyrotoxicosis. The iodine treatment of thyroid cancer has history for over 50 years [10]. Other important method are the treatment of polycythaemia vera (hyperfunction of bone marrow for unknown reason) and other bone marrow therapies with ^{32}P [17]. A review of the several treatment techniques is given in [17] and a more detailed presentation of iodine treatments in [10].

1.1.2 Properties of therapeutic nuclides

In 1991 there were nearly 50 radiopharmaceuticals with different targeting mechanism available for therapy. All isotopes that are used in TRT emit particle radiation, that is, α or β^- particles, whose energy is absorbed in the surrounding tissue in very short distance. The β^+-emitters (positron emitters) are not used in TRT because of the annihilation into two 511 keV photons which have long range and therefore add the undesirable dose to the healthy tissue. Energy of the electrons absorbs into the tissue in short distance ($\sim$ 1-10 mm), which makes it possible to target the tissue destroying effects in desirable volume.

Most of the applied nuclides also emit photons which add background dose to other parts of patients body. These photons, however, make it possible to monitor the activity distribution in the target with radioisotope imaging. Unfortunately the intensity and the energy of the emitted photons is too high for ordinary gamma-camera. Also, the photon spectrum usually includes several energies with high intensity, which makes the efficient scatter correction difficult when the observed energy is not the highest of the emitted energies.

1.1.3 On the importance of on-therapy imaging

Determination of the delivered dose in the tumor requires information about the distribution of the therapeutic nuclide. One approach is to use so called Medical Internal Radiation Dose or MIRD formalism, which is based on experimental values of nuclide mobility and accumulation in tissues. All values in MIRD approach are approximations for reference patient and the results can differ from the true values. The principles of dose calculation in MIRD formalism are given in [3] and an application to ^{131}I-treatments in [43]. Another way to calculate the tumor dose is to measure (image) the distribution of active nuclide and calculate the dose based on this distribution. This approach, of course, takes into account the patient-dependent distribution of radiopharmaceutical and anatomy of the patient. Because the uptake of the radionuclide can vary between patients, imaging of the activity distribution is necessary to obtain reliable results.

The uptake of ^{131}I is affected by patient's medication and diet. Thyroid hormone (thyroxine) treatments should be paused for a month before administration of therapeutic dose of ^{131}I. Also iodine containing foods should be avoided, e.g. sea fish and cough mixtures. Furthermore, the contrast mediums used in X-ray imaging inhibit the localization of iodine in the thyroid.

For thyrotoxicosis the administered dose is usually between 300-370 MBq. Dosage will be estimated by physician with respect to the size of thyroid and pre-treatment uptake measurements of ^{123}I with gamma-camera (planar scintigraphy). In the case of thyroid carcinoma, doses range from 3.7 to 5.5 GBq, but can rise up to 11 GBq, depending on the difficulty and the prevalence of the disease. [36, 38, 37]

Pre-treatment uptake measurements are used to determine the efficiency of the treatment and to approximate the tumor dose with respect to the administered dose of ^{123}I. Patients with thyroid cancer are whole-body imaged four or five days after the treatment to detect the metastases in other parts of the body [37]. These methods, however, do not give quantitative information about the dose in the tumor and consequently, there is a need for quantitative imaging method.

1.2 Radioisotope imaging

Scintillation cameras are used to get a planar image of the activity distribution inside the patient. The planar image can be considered as a two-dimensional projection of the three-dimensional distribution. The main parts of the scintillation camera are the collimator, the scintillation crystal and the photomultiplier tubes. (see Fig. 1.1) The purpose of the collimator is to block out all photons that are non-parallel to it's holes. The holes of the collimator can be parallel, diverging, converging or the collimator can consist even of one small hole (pin-hole collimator). In this thesis we discuss only parallel-hole collimators. When a photon passes through a collimator hole it can be absorbed in the scintillation crystal. Absorption of the photon produces an light flash of visible wavelength in crystal.

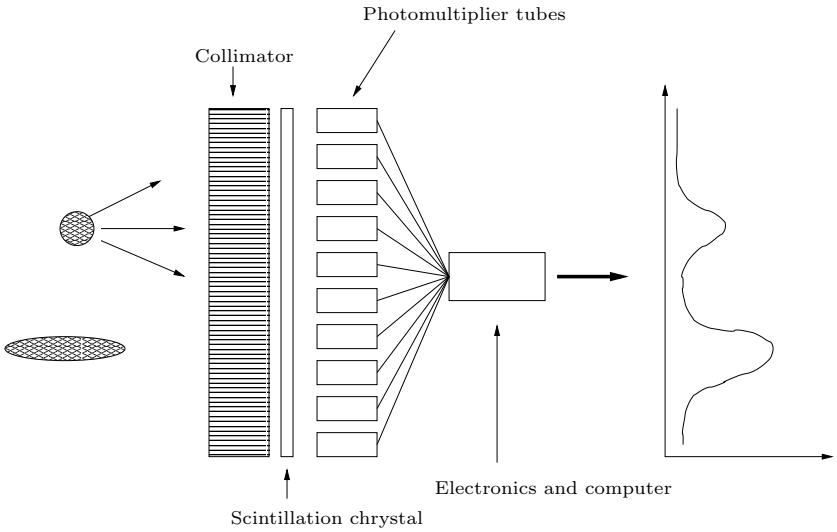

Figure 1.1: Principle of scintillation camera

The emitted visible light is then detected by the photomultiplier tubes. The output of the photomultipliers is proportional to the amount of the detected photons. The intensity of radiation is inversely proportional to the square of the distance from the source and therefore one can determine the (x, y)-coordinates of the light emission based on the outputs of several photomultipliers which detect different light intensities at different distances. Also the energy of the absorbed gamma-quantum can be determined from so called z-pulse.

The collimators transfer the location information in imaging area to location information in scintillation crystal. In ideal case, when collimator holes are of infinite length, one row of the planar image corresponds to projection of one thin slice (height same as the collimator hole diameter) of the activity distribution. This approximation is made in the image reconstruction in most of the clinical SPECT-systems. With this approximation the formation of the one row on the planar image can be written as an line-integral:

$$P_\theta(t) = \int_{I_{t,\theta}} f(x, y) dI, \tag{1.1}$$

where θ is the projection angle, $f(x, y)$ the object function (activity distribution), $P_\theta(t)$ the value of projection at point t and $I_{t,\theta}$ denotes a line passing through image plane and having direction parallel to the collimator holes. However, the collimator is never ideal and moreover, there are interactions between the gamma-quantum and the medium. As a consequence, the model (1.1) is not correct, the finite dimensions of collimator, the attenuation, the scatter and the statistic nature of the radiation affect to the observations and should be modeled. Image degrading processes in SPECT are discussed in [4] and [9]. The modeling of imperfect collimator response and attenuation are discussed in Section 2.2.

When sufficient amount of photons are detected the planar image can be produced. Normally it is a pixel map in which each pixel corresponds to certain area in (x, y)-coordinates and it's value to the number of detected photons in that area. The z-pulses are used to determine if a detected photon is a scattered or a primary photon. In each interaction (usually Compton scatter) with medium, photon loses some amount of energy and changes the direction of propagation. Thus, scattered photons may be detected even if they were not originally parallel to the collimator holes. Since the z-pulse is proportional to the energy of absorbed photon, the photons that have lower energy can be neglected in image formation by setting a cut-off value for the z-pulse. This, of course, does not remove all scattered photons from the image data. Usually the energy window of accepted pulses is 10-20 % wide and photons that lose less than that amount of energy in scatter process will be included in the planar image.

Since the detection of the absorbed photons requires electronics there is a small dead-time in scintillation camera. This is the time when the electronics can not respond to the signals from absorbed photons before the information from previous absorption is processed. Dead time is not significant when imaging diagnostic activities but becomes more critical when therapeutic doses are imaged and count rates are high.

One should also notice that there is only one scintillation crystal which must detect all photons in planar image in gamma-camera. Usually the planar image consists of 128×128 pixels when at the same time in diagnostic collimator there are as many as 89 000 holes. This implies that the number of detected photons in each projection (planar image) pixel is superposition of photon penetration from several collimator holes. This effect is not considered in the modeling of the observations (Section 2) since all measurements in this thesis are done with 6P-SPECT where each collimator hole produces one projection pixel.

All current devices are optimized for diagnostic purposes, that is, for imaging low activities of ^{99m}Tc, ^{123}I etc., whose photon energy is about 150 keV. The requirements of the diagnostic imaging are different from the needs of on-therapy imaging. The main differences are the high activity and the high gamma-energy of the isotopes used in radionuclide therapy.

1.3 Single photon emission computed tomography SPECT

In tomographic imaging the goal is to reconstruct the three-dimensional estimate of the activity distribution based on several planar images acquired in different angles around the object. The planar images of the activity distribution are obtained by the scintillation camera. Often the reconstruction of the activity distribution is performed only in two dimensions and the three-dimensional effects are ignored. (see Figure 1.2). The *forward problem* in SPECT is the construction of model, that can be used to calculate the projections to measurement angles, when activity distribution is known. Eq. (1.1) is a coarse approximation of the formation of projection. When the problem is modeled properly, all the physical properties affecting the imaging are included in the observation model. The effects include collimator response, attenuation, scatter, septal penetration, statistics of the radiation etc.. In addition, the observation model must be discretized since the reconstruction can not be performed analytically when problem is modeled properly. When linear observation model is used, we can write for the formation of projections the following equation:

$$P = Rf, \tag{1.2}$$

where P is the vector of projection pixels corresponding to all measurement angles, f is the vector including the discretized values of the activity distribution and R is the linear observation model.. The construction of R is described in Chapter 2.

When R is known the reconstruction of activity distribution can be written formally as

$$f = R^{-1}P, \tag{1.3}$$

where R^{-1} stands for inverse operator of R. Equation (1.3) is known as the *inverse problem* of SPECT. The inverse operator of R does not actually exist but there are several methods for reconstruction of the activity distribution. Main methods are described in Chapter 3.

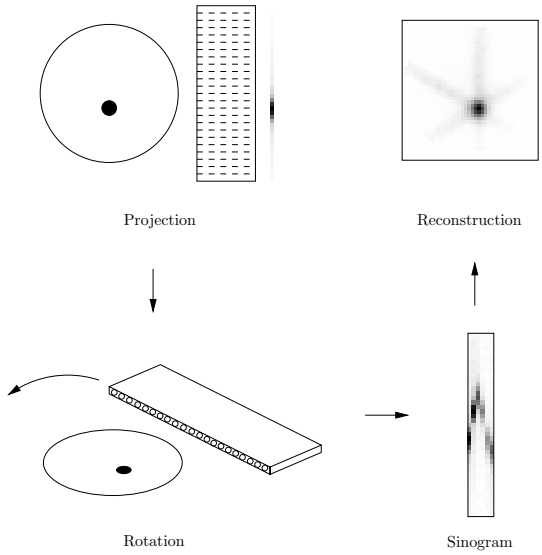

Figure 1.2: Principle of SPECT imaging. First, the projection to angle θ_i is acquired, and then the scintillation camera is rotated around the object. When all desired projections are measured, the reconstruction is done using the combined projection data.

1.4 Imaging of targeted radionuclide therapy

As explained in previous sections, the development of clinical radioisotope imaging systems is based on diagnostic needs and thus the equipments are not suitable for imaging high activity levels and high-energy photons. Although there are several different techniques for imaging radionuclide treatments, only few give accurate quantitative information about the activity distribution in body. Review of currently used imaging methods is given in [39].

1.4.1 Existing techniques

Rectilinear scanners and *Planar scintigraphy* can be used to determine the whole-body or regional localization of radiopharmaceutical. In rectilinear scanner a focused collimator is attached to a large volume NaI-scintillation crystal. The hole body imaging is achieved by scanning the detector across the surface of the patient. The thick scintillation crystal gives good detection efficiency of high-energy photons.

In planar scintigraphy similar gamma camera as in SPECT is used to measure only one projection of activity distribution. With a gamma camera large area can be imaged at once, but naturally this method has the same disadvantages concerning the detector system as SPECT. On-therapy imaging requires high-energy collimators and also lead filter has been used in the front of the collimator to reduce high count rates [42, 15]. Use of lead filter increases the effect of scattering in observations and therefore blurs the image. Lead filtering and high-energy collimators add weight to the gantry. This extra weight in gantry can cause incorrect positioning of the camera head and therefore produce artifacts in the images.

Four or five days after the administration of therapeutic dose when the count rates are low enough but tumors are still highly active, planar scintigraphy can be used to point out unknown metastases. Rectilinear scanner and planar scintigraphy can be calibrated using phantoms to obtain approximate quantitative results.

Positron emission tomography (PET) is not suitable for therapy imaging due to the high efficiency of positron cameras. However, since PET has the highest spatial resolution of all radioisotope imaging devices, it is ideal for pre-therapy imaging and therapy planning using pharmacoki-

netics.

1.4.2 6P-SPECT

6P-SPECT stands for *Single Photon Emission Computed Tomography from 6 Projections*. The imaging device consist of six one-row collimators, heavy enough to deal with high activities and high gamma-energies associated with TRT (see section 5.1). Using the six projections it is possible to reconstruct one slice of the three-dimensional activity distribution. Due to the very limited number of observation angles the spatial resolution of 6P-SPECT is not comparable to the resolution achieved with clinical gamma cameras. It was shown in [28], that the relative activity distribution obtained with 6P-SPECT can be converted to absolute activity distribution by surface dose measurements (Section 4.2). Furthermore, the absolute activity distribution can be used to calculate the absorbed dose in critical organs and tumors

The 6P-SPECT imaging system was designed [28] to have simple structure and to be able to detect high activities and photon energies used in targeted radionuclide therapy. Since the photon energies associated with radionuclide therapy are higher than in normal SPECT imaging, efficient collimation is needed. The loss of detected photons due to efficient collimation does not cause problems since the activities are high in the case of radionuclide therapy.

In 6P-SPECT the projections are acquired in all six directions simultaneously and no rotation is needed. The measurement system consists of six one-row collimators each having 41 holes. Collimators are placed in hexagonal form around the object to be imaged. In the cited study thermoluminescence dosimeters (TLDs) were used as detectors, so that one TLD pellet was placed in each collimator hole. TLDs are integrating detectors which measure the radiation dose. As stated in [28] the sensitivity of the TLDs is low, and thus in their study the acquisition time for 2.5 GBq phantom was 24 hours which is clearly not suitable for a clinical application. On the other hand the use of TLDs speeds up the acquisition since all the projections can be measured simultaneously. A disadvantage compared to the scintillation crystals is lack of energy resolution, that is, all the scattered photons -in addition to primary photons- reaching the TLD pellet are detected.

In this thesis we measured the projections using a small scintillation crystal attached to one photomultiplier tube and one-channel analyzer. The details of measurements are shown in Section 5.1.

Figure 1.3: Three 6P-SPECT collimators. If TLDs would be used as radiation detectors, all projections could be measured simultaneously.

1.5 Aims of the thesis

This thesis is a continuum for the thesis [44] in which the modeling and the computational issues of SPECT were considered. In this study the computational methods are developed further.

There are three aims in this thesis. First different SPECT activity reconstruction algorithms and observation models are discussed and compared. Then the calculation of dose distribution

based on the reconstructed activity distribution is considered. Finally phantom studies are performed to evaluate the activity reconstruction and dose calculation with real measurement data.

When modeling the measurements we consider especially the case of 6P-SPECT. Because of the very limited number of observations, the adequate modeling of the measurements is crucial for efficient activity reconstruction. In addition to correct modeling, modern class reconstruction methods must be used to obtain reliable results.

Two different types of phantoms are used in experimental part of the study. First a water phantom is used in measurements, which aim to evaluate the efficiency of the reconstruction of the activity distribution. The accuracy of the dose calculation is verified using a Lucite phantom for simultaneous projection and dose profile measurement. Dose profiles are measured with several TLD pellets inside the phantom.

Chapter 2

Modeling of observations in 6P-SPECT

In most of the SPECT systems that are in clinical use the activity distribution is reconstructed using the Filtered Back Projection (FBP). The ordinary FBP (see Section 3.1) does not concern any physical or geometrical properties of the measurement scheme. However, there are modifications of the FBP for including attenuation in the reconstruction. Also methods for approximating the effect of the collimator blur by selecting a proper filter have been suggested. In the methods that are based on Filtered Back Projection the back-projected distribution can be corrected in several ways, for example, scatter-, attenuation and collimator corrections can be added to the image. These corrections include the known physical and geometrical properties of the imaging system [9].

A more sophisticated approach for image reconstruction is to construct a model for the observations, known as the forward problem, and then to use suitable inversion methods in order to compute the activity distribution based on the observations. The forward model should include all the physical features related to acquisition. In this chapter we consider two of these, the effect of imperfect collimator response and attenuation. Later, in Section 3.3 we consider the statistical properties of radioactive decay. The modeling of the measurements is discussed in e.g. [40, 44, 6] and [2].

2.1 Observation model in the case of additive noise

In the two-dimensional case, only one slice with the activity distribution $f = (f_1, \dots f_{N_x N_y})^{\mathrm{T}} \in \mathbf{R}^{N_x N_y \times 1}$ is reconstructed at $N_x N_y$ pixels, usually the reconstructed slice is a square of N^2 pixels, where N is the width of the slice in pixels. We can denote the projection vector with $P = (p_1, \dots, p_b)^{\mathrm{T}} \in \mathbf{R}^{b \times 1}$ where $b = LM$. L is the number of projection bins in one projection and M is the number of projection angles. In two-dimensional observation model it is assumed that all of the detected photons are emitted from a single plane which is at the same height as the row of collimator holes.

If we use linear additive noise model, the observation equation for a single projection bin will be

$$p_i = \sum_{j=1}^{N^2} H_{ij} f_j + v_i, \tag{2.1}$$

where p_i is the number of detected photons at projection bin i, H_{ij} is the probability that a photon emitted from the center of the pixel j will be detected at projection bin i, f_j is the total number of emissions from the pixel j and v_i presents the Gaussian noise from the detector electronics etc. The summation is done over all image pixels f_j. In the matrix form the observation equation is

$$\begin{pmatrix} p_1 \\ \vdots \\ p_b \end{pmatrix} = \begin{pmatrix} H_{11} & \cdots & H_{1N^2} \\ \vdots & \ddots & \vdots \\ H_{b1} & \cdots & H_{bN^2} \end{pmatrix} \begin{pmatrix} f_1 \\ \vdots \\ f_{N^2} \end{pmatrix} + \begin{pmatrix} v_1 \\ \vdots \\ v_b \end{pmatrix}, \tag{2.2}$$

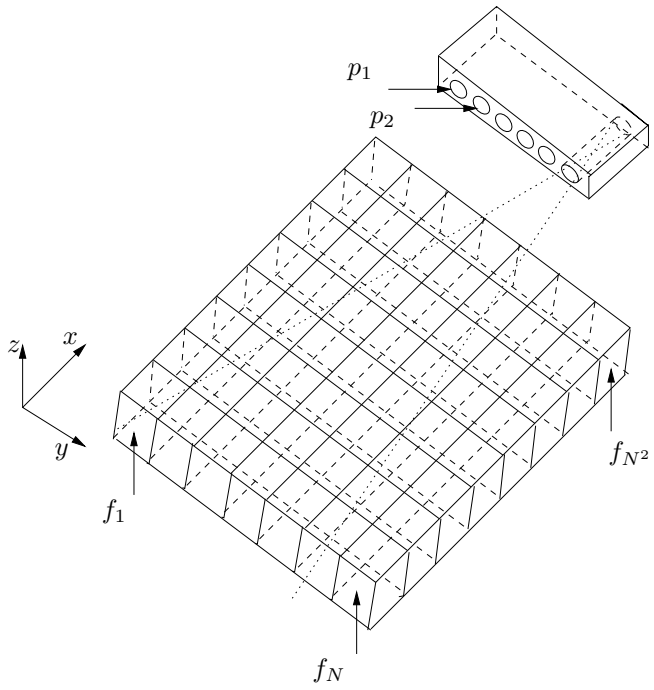

Figure 2.1: 2D-model. Only one plane is reconstructed.

or

$$P = Hf + v. \tag{2.3}$$

Here P s the combined projection vector, f the vector of activities in image pixels and matrix H is called the *observation matrix*. The elements of observation matrix $H \in \mathrm{R}^{b\times N^2}$ are defined in a way that the element H_{ij} is the probability that a photon emitted from j^{th} pixel is detected by i^{th} projection bin. The construction of the observation matrix H is considered in the next section. Since collimator holes are circular, each projection bin can detect photons that are emitted inside a cone-shaped volume. The detector system itself measures projections only in one plane but the three-dimensional activity distribution should still be concerned. For 3D-reconstruction we must discretize the whole volume that is "visible" for projection bins, slice by slice. If we set the number of pixels in one slice to N^2 and the number of slices to N_z, the activity distribution vector will be of size $f = (f_1 \dots f_{N_x N_y N_z})^{\mathrm{T}} \in \mathbf{R}^{N_x N_y N_z \times 1}$. In our models N_z is always odd number, that is, the center plane is equal to the 2D-reconstruction plane and there are $(N_z - 1)/2$ planes at both sides. Here we have only the same number of projections as in 2D-case and the dimensions of the observation matrix will be $H \in \mathrm{R}^{b\times N_x N_y N_z}$. In 3D-case the observation matrix consists of N_z blocks:

$$H = \left[H_{-\frac{N_z-1}{2}} \cdots H_{\frac{N_z-1}{2}} \right], \tag{2.4}$$

which each corresponds to a x, y-plane in z-direction. Each H_i is of size $(b \times N^2)$.

When the observation model (2.3) is formed and the data P is given, the activity f can be reconstructed by solving a (regularized) LS-problem, see Section 3.2. The elements H_{ij} of the observation matrix are also needed in the case of maximum likelihood estimation discussed in Section 3.3, although the observation model is not of the linear form (2.3) when the Poisson-statistics of radiation is taken into account.

2.2 Modeling of the detector system

When the problem is modeled correctly, the observation matrix H includes all physical properties of the detector system. The four main features that should be taken into account when modeling the system are collimator blurring, attenuation and scattering. These three phenomena can be included in the observation matrix H. Fourth property of the SPECT, the Poisson statistics of the radiation, can be taken into account in the reconstruction when statistical inversion theory is used (see Chapter 3). In this section we consider modeling of the collimator response and attenuation. Here we mainly follow the guidelines of the thesis [44]. As in [44], scattering and septal penetration are not taken into account.

Scattering could be modeled using Monte-Carlo calculations or alternatively it can be reduced in clinical SPECT-systems by using multiple energy-windows during projection imaging. Scatter modeling is discussed for example in [2, 26, 12, 23, 40] and [48].

Modeling of the detector system is considered in [40, 44, 6] and comparison between the effects of scatter, collimator blur and attenuation in [12].

2.2.1 Interpolation method

Before showing the modeling of the collimator response and attenuation, we introduce a method that is used to speed up the construction of the observation matrix H. For forming the observation matrix we use the interpolation method described in [44]. This method is based on the idea that the rotation of detector system around the object is equivalent to rotation of the object in the coordinates fixed to the detector system. Consider, for example the 2D observation matrix H that consists of M blocks each corresponding to one acquisition angle. In the interpolation method we first form so called *zero-angle observation matrix* H_0, that is a model for formation of projection at acquisition angle $\theta_0 = 0°$. Let $C_k \in \mathbf{R}^{N^2 \times N^2}$ be an *interpolation matrix* which rotates the activity map to angle θ_k. Then the projection $P_k \in \mathbf{R}^L$ to angle θ_k can be written in the form

$$P_k = H_0 C_k f, \tag{2.5}$$

thus the observation matrix H can be written as

$$H = \begin{pmatrix} H_0 C_1 \\ \vdots \\ H_0 C_M \end{pmatrix}. \tag{2.6}$$

In the 3D-case the observation matrix H is constructed basically as in 2D case. The only exception is that now the distribution f needs to be rotated in *each plane*. Consequently, if we denote the zero-angle observation matrix corresponding to plane k by $H_{0,k}$, the observation matrix H gets the form

$$H = \begin{pmatrix} H_{0,-\frac{N_z-1}{2}} C_1 & \dots & H_{0,\frac{N_z-1}{2}} C_1 \\ \vdots & \ddots & \vdots \\ H_{0,-\frac{N_z-1}{2}} C_M & \dots & H_{0,\frac{N_z-1}{2}} C_M \end{pmatrix}. \tag{2.7}$$

In all of the calculations in the Chapter 5 we use bilinear interpolation method in the rotation of the pixel map. This method has also a drawback that is discussed in Section 2.3.1.

2.2.2 Modeling of the collimator

Next we consider three dimensional modeling of the collimator response. The observation in 6P-SPECT are not actually projections of the activity distribution. That is, instead of being line integral defined by Eq. (1.1), the projection bins p_i consists of counts caused by photons emitted from a 3D cone. In this Section we model the collimator effect without medium. The effect of attenuation is incorporated into the model later in Section 2.2.3.

In the two-dimensional observation model the activity distribution is assumed to be in 2D but the collimator holes can be modeled in 3D. For detailed derivation of 3D collimator model see [44]. The collimator model for transmission imaging is shown in [50].

The first task is to form the collimator modeled zero-angle observation matrix. After that the observation matrix can be constructed using the interpolation method described in section 2.2.1. The activity distribution is discretized by approximating that the activity of a voxel is concentrated in the center of the voxel.

The elements of the zero-angle matrix $H_0(i,j)$ are the probabilities that a photon emitted from the point source at the center of the voxel j is detected at the projection bin p_i. This probability is proportional to the solid angle φ_{ij} subtended by the visible part of the projection bin p_i to the pixel j, that is

$$H_0(i,j) = \frac{\varphi_{ij}}{4\pi}. \tag{2.8}$$

Furthermore, the solid angle φ_{ij} is

$$\varphi_{ij} = \frac{A}{\|\overline{d}\|^2} \tag{2.9}$$

where $\overline{d}$ is the is vector pointing from the center of the outer end of collimator hole i to the center of pixel j, (see Figure 2.2), and A is the area of the projection bin "seen" by the voxel j, projected to the direction $\overline{d}$.

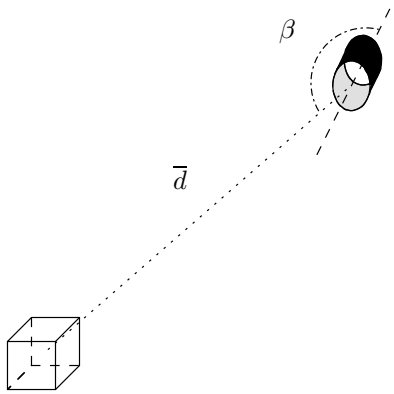

Figure 2.2: The angle β between a collimator hole and a voxel.

The calculation of the visible area A is straightforward, here we show only the equations, that are required for the collimator model, see details from [44]. With an approximation $d >> h$, A is determined by two intersecting ellipses with equal axes. The ellipses are the projections of the both ends of the collimator hole to the direction of the voxel j. If we denote the radius of collimator hole with r, length of the hole with h and a vector pointing from center of p_i to the center of the other end of the collimator hole with $\overline{n}$, the angle β between vectors $\overline{d}$ and $\overline{n}$ can be calculated as:

$$\beta = \arccos\left(\frac{\overline{n}\cdot\overline{d}}{|\overline{n}||\overline{d}|}\right). \tag{2.10}$$

For parallel beam collimators $|\overline{n}| = h$. By setting $b = r\cos\beta$ and $k = h\sin\beta$, the area of the visible part of projection bin can be written as

$$A = 4\left(\frac{b}{r}\left(\frac{x_a}{2}\sqrt{r^2 - x_a^2} + \frac{r^2}{2}\arcsin\left(\frac{x_a}{r}\right)\right) - \frac{k}{2}x_a\right), \tag{2.11}$$

in which x_a is the x-coordinate of the intersection points $(-x_a, y_a)$ (x_a, y_a) of the two ellipses:

$$x_a = r\sqrt{1 - \frac{k^2}{4\beta^2}}. \tag{2.12}$$

The zero-angle observation matrix can be calculated using (2.8). When A is negative, photons emitted from current voxel can not be detected at the projection bin. This model does not take into account the septal penetration, instead it assumes total attenuation in hole walls. In practice, however, some amount of detected photons at particular projection bin have passed the septa. This phenomena, of course, causes an inaccuracy in the observation model.

The above described model is three dimensional. However, the same model can also be used in 2D model, simply by considering voxels only in one layer.

2.2.3 Modeling of attenuation

We consider modeling of attenuation in that case when the attenuation map is assumed to be known. Another approach is to take both attenuation and activity distributions as unknown functions and to estimate these functions simultaneously based on observations of SPECT. In this approach both transmission and emission algorithms are combined and the reconstructed activity distribution is used as the source for the transmission algorithm. Both least-squares [11] and maximum likelihood [27] scheme have been considered in literature.

The intensity of radiation obeys the exponential attenuation law

$$I = I_0 e^{-\int_l \mu dl}, \tag{2.13}$$

where I is the intensity of radiation at the depth l in medium, μ is the linear attenuation coefficient of the medium and I_0 is the initial intensity of radiation.

To include the effect of homogeneous attenuating medium in observation matrix, each element of H_0 must be multiplied by the exponential term of Equation (2.13) with a corresponding distance l. The value of l is then the distance between the center of the pixel f_j and the edge of the medium along a straight line from the pixel to the center of the projection p_i (so called *radiological path*).

In the case of inhomogeneous medium the attenuation coefficient can vary between pixels and therefore we write counterpart of the Equation (2.13) in a form

$$I = I_0 e^{-\sum_m \mu_m l_m}, \tag{2.14}$$

where the summation is made over all pixels that the radiological path described above intersects. The terms μ_m and l_m refer to the linear attenuation coefficient of pixel m and the length of the intersection with pixel m, respectively. Later we will refer to this attenuation model as inhomogeneous attenuation.

The lengths l_m can be calculated using method described in [46] where the pixels (or voxels) are considered as intersection areas of a set of orthogonal planes rather than individual elements. The resulting algorithm is exact and efficient, since the required computer times is proportional to the number of planes, not to the number of pixels. We use a slightly modified version of the algorithm.

The interpolation method described in Section 2.2.1 can also be applied to attenuation correction. First we define the attenuation matrix Γ by equation

$$\Gamma_{i,j} = e^{-\sum_m \mu_m l_{mij}}, \tag{2.15}$$

where i, j refer to the source and projection pixels and m to the intersected pixels. This matrix incorporates the effect of attenuation in the direction $\theta_0 = 0°$. In order to compute the block of the observation matrix H corresponding to angle θ_k we first rotate the attenuation map μ to that angle with the interpolation matrix C_k, so that

$$\mu^k = C_k \mu, \tag{2.16}$$

where μ^k is the rotated map.

Then the attenuation matrix Γ^k, corresponding to the angle θ_k, can be calculated as in Equation (2.15) by replacing the attenuation map μ with the rotated attenuation map μ^k. Now the elements of Γ^k correspond to the attenuation effect of the pixels in the direction θ_k. Finally, the attenuation

modeled 2D observation matrix can be formed like in Equation (2.6), but now we must multiply each block with the corresponding attenuation matrix:

$$H = \begin{pmatrix} (H_0 \odot \Gamma^0)C_1 \\ \vdots \\ (H_0 \odot \Gamma^M)C_M \end{pmatrix}. \tag{2.17}$$

Here $\odot$ stands for element-by-element multiplication of matrices. In 3D-model each of the N_z blocks -corresponding to N_z planes- is formed as in Eq. (2.17) and then the observation matrix can be constructed using Eq. (2.4). In this study we make the following approximation in the case of 3D attenuation. We assume that the pixels that have the same (x, y)-coordinates have the same attenuation coefficient, in the other words, we assume that the attenuation distribution is homogeneous in z-direction. The effect of attenuation correction is demonstrated in Figure 2.3.

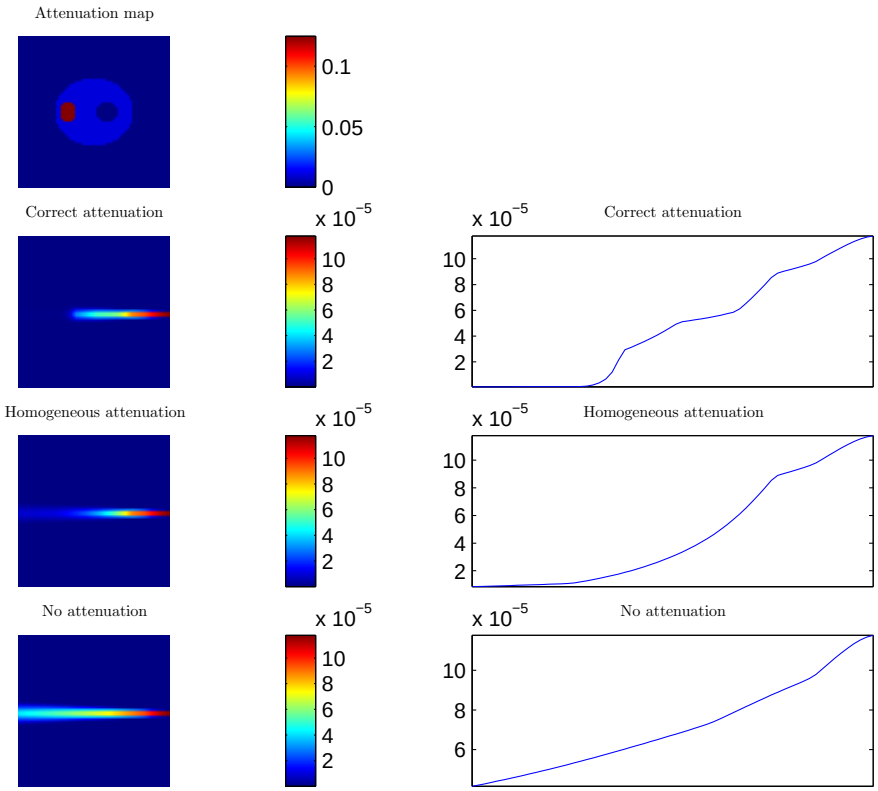

Figure 2.3: Observation models with different attenuation corrections. The simulated attenuation map at the top left presents the linear attenuation coefficients of the object. In the first column one row of each of the different observation matrices is illustrated. Pixel values represent the probabilities that a photon emitted from each pixel will be detected at the fixed projection bin. The plot in the second column represent the profiles of the images on the first column, at direction parallel to the collimator hole. Loosely speaking, the images illustrate the field of view of the projection bin in question in the case of different observation models.

2.3 ROI-Reconstruction, reduction of parameters

Usually in image processing applications selecting a *Region Of Interest* or ROI means that an area of the image is selected. Then this part of the image is processed or a mathematical operation is

done to the pixel values in this area. For example in SPECT imaging one could be interested in the total activity in certain part of the image. Then this area could be selected and the activity values integrated over all pixels that belong to the selected area. In addition, ROI selection can be used for parameter reduction. The purpose of parameter reduction is to minimize the required computer time.Description of method for reconstructing only total activity of selected ROI is given in [18].

Here we use the term ROI in slightly different sense: we select areas that are not interesting, that is, areas that do not contain any sources. Shortly, we first select these areas where should not be any sources and then manipulate the observation matrix H so that the activity of the ROI is taken on a single reconstruction parameter in the observation model. In other words all pixels in the selected area are assumed to have same activity. With this procedure the number of reconstruction parameters decreases and some artifacts can be reduced.

Here we consider a method of selecting ROI's prior to reconstruction and including them in the observation model in matrix form as in [24]. This method is illustrated for observation model that operates on two-dimensional activity distribution and generalization for three-dimensional case is shown.

2.3.1 Effect of ROI selection

The ROI-model is considered here in order to avoid an estimation error resulting from the use of the interpolation method (see Section 2.2.1) in calculating the observation matrix H. The interpolation method cuts the rotated map to the same size as the original. Illustrative way to see the problem is to look at the columns of the observation matrix. The i'th row of the observation matrix corresponds with the pixels that will be detected by the i'th projection bin. In Figure 2.4 are illustrated, loosely speaking, the field of views of single collimator hole in different projection angles. One way to avoid this problem is to select one circular area at the center of the slice and force all pixels in the outer part of it to be of equal activity. This can be done when we know that there are no sources outside the selected area.

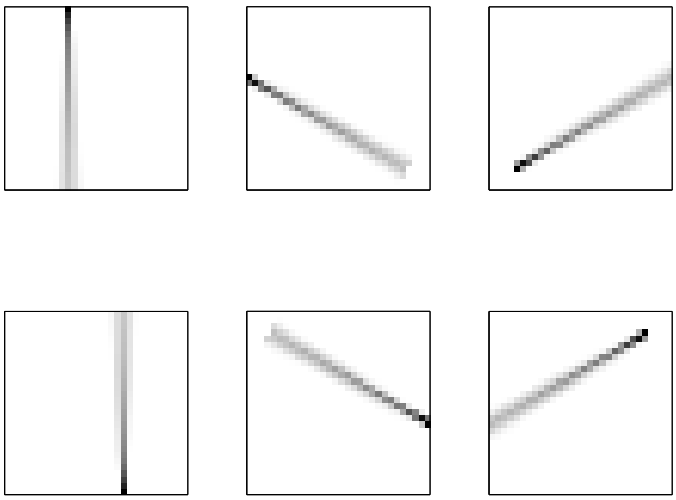

Figure 2.4: Reshaped rows of collimator modeled observation matrix. Each image represents pixels that are visible to a fixed projection bin at different angles in 30×30 slice.

The ROI selection also regularizes the inverse problem in activity reconstruction. The normally highly underdeterministic model becomes more stable when the number of parameters is reduced by the ROI selection. Including of the ROI-selection in the observation model can be considered as incorporation of *a priori* information of the activity distribution in the problem. ROI-selection

is a hard prior, it assumes that the selected ROI's are in constant activity and therefore the use of such a model must be well reasoned.

2.3.2 ROI-model in two-dimensional case

Let us denote the vector including the activities in q ROI's by $\phi \in \mathbf{R}^{q\times 1}$. Later we refer to this vector ϕ as the reduced activity distribution, since q is is lower than the number of pixels in the original discretization of the activity f. Our goal is to form a matrix $R \in \mathbf{R}^{N^2\times q}$, which transforms the reduced activity distribution to its original size, that is

$$f = R\phi. \tag{2.18}$$

The ROI-matrix R is formed as follows: The i'th column of R corresponds with i'th ROI-area, and thus there are 1's in the rows with indices of the pixels belonging to the i'th ROI, and all other elements in the column are zeros. That is, the i'th column of R is a index set of pixels that belong to the i'th area. When the ROI's are disjoint, the areas in pixels of the q ROI's are given by the diagonal elements of matrix $R^{\mathrm{T}}R$.

Now we can write constrained observation model which includes the ROI-selections:

$$P = Hf + v = HR\phi + v = \widetilde{H}\phi + v, \tag{2.19}$$

where $\widetilde{H}$ is the observation matrix associated with the ROI constrained observation model. In the observation model (2.19) the number of unknown parameters is reduced to q, the number of ROI's. It is also worth to notice that any are can also be reconstructed pixel by pixel, simply by choosing ROI's that are of the size of one pixel only. Thus, the original problem can be restored by selecting $R = I$, an identity matrix.

Integration, or in this discrete case summation, of the activities over ROI's can also be computed as a matrix product using the same matrix:

$$\vartheta = R^{\mathrm{T}}f \tag{2.20}$$

where $\vartheta \in \mathbf{R}^{q\times 1}$ is a vector containing the integrated activities of the original activity distribution f over the selected areas.

As an example of constructing the ROI matrix R we show a sample case with 3×3 grid. Figure 2.5 represents a grid with three different areas with different colors. For reconstruction, where each area has constant activity (ϕ_1, ϕ_2, ϕ_3), we must form a 9×3 ROI-matrix R as described before. The relation between reduced parameters and f according to Eq. (2.18) will be

$$f = \begin{pmatrix} \phi_1 \\ \phi_2 \\ \phi_1 \\ \phi_2 \\ \phi_3 \\ \phi_2 \\ \phi_1 \\ \phi_2 \\ \phi_1 \end{pmatrix} = \begin{pmatrix} 1 & 0 & 0 \\ 0 & 1 & 0 \\ 1 & 0 & 0 \\ 0 & 1 & 0 \\ 0 & 0 & 1 \\ 0 & 1 & 0 \\ 1 & 0 & 0 \\ 0 & 1 & 0 \\ 1 & 0 & 0 \end{pmatrix} \begin{pmatrix} \phi_1 \\ \phi_2 \\ \phi_3 \end{pmatrix}. \tag{2.21}$$

As a second example we show a case where a circular area at the center of the slice is selected and activity is assumed to have a constant value outside the circle. Thus, in reconstruction we choose the ROI's inside the circle to be of the size of one pixel and the outer part of the image is considered as one ROI.

We will use real measurement data and attenuation and collimator corrected observation matrix. By selecting the ROI as described, the number of reconstruction parameters is reduced and the artifacts are decreased. The ROI and the reconstructions in addition with the sparsity structure of the observation matrix $\widetilde{H}$ are shown in Figure 2.6.

2.3.3 Three-dimensional case

As shown in Section 2.1, in three-dimensional case observation matrix consist of N_z blocks, each corresponding to one z-plane:

$$H = \begin{bmatrix} H_{-\frac{N_z-1}{2}} & \cdots & H_{\frac{N_z-1}{2}} \end{bmatrix} \tag{2.22}$$

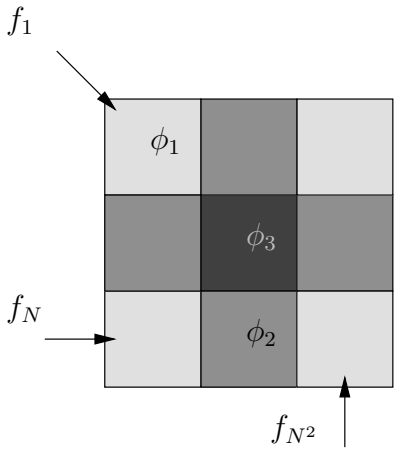

Figure 2.5: 3×3 grid

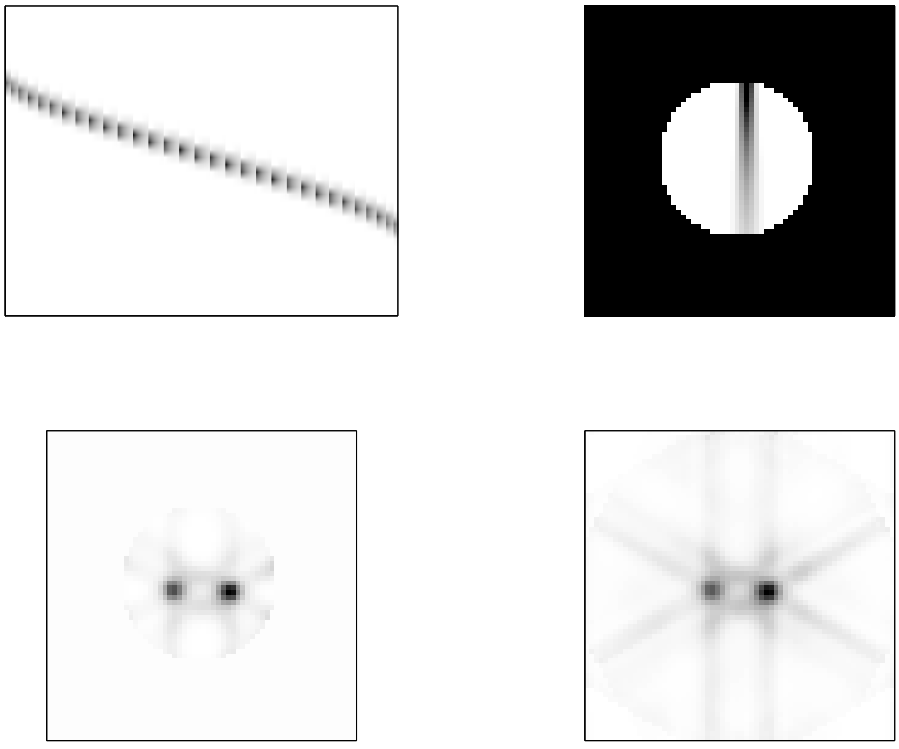

Figure 2.6: Examples of ROI-model. At the top left is visualized 42 first rows of the ROI-modeled observation matrix.. At top right is shown the "field of view" of a fixed collimator hole. At the bottom left is shown reconstruction with ROI-selection and at bottom right reconstruction with normal observation model. Both reconstructions are calculated using maximum likelihood estimates (Section 3.3).

where size of H_i is $b \times N^2$. In order to select the ROI's in all planes, we must multiply each block with ROI matrix R. Consequently in every plane the number of reconstruction parameters is reduced to q. The construction of the ROI matrix R is equal to the 2D-case and the the observation matrix, which includes the ROI-selections in three dimensions, can be formed as

$$\widetilde{H} = \left[H_{-\frac{N_z-1}{2}} R \ \cdots \ H_{\frac{N_z-1}{2}} R \right] \tag{2.23}$$

Actually this construction method gives us a possibility to select different ROI's in different planes by using individual ROI matrices for each z-plane.

2.3.4 $2\frac{1}{2}$-D model

With 6P-SPECT projections are acquired in one z-plane only. The 3D model takes into account all z-planes in which any of the voxels are visible to projection bins. Thus, without any ROI-selections the number of reconstruction parameters is $N_z N^2$ as the number of observations in 6P-SPECT is fixed at 246 (41 projection bins per projection, six projections). Consequently, the 3D model is highly underdeterministic. Another problem is that in the 3D model some voxels are detected only in single projection due to the cone-shaped field of view of the projection bins. These aspects make the accurate, fully three dimensional, reconstruction in 6P-SPECT impossible.

Here we show a modification of the three-dimensional observation model which assumes activities at the same xy-coordinates to be equal in z-direction. That is, this model takes into account the three-dimensional activity distribution and collimator model but with assumption that there is no variation in the activity distribution in the z-direction. We call this model the $2\frac{1}{2}$D model. An alternative approach to regularize the reconstruction with respect to the z variation is to approximate the point spread function in z direction with constant function derived from fully 3D model [6].

In order to form the $2\frac{1}{2}$D model we first calculate the height of the volume that effects the projections. We will make the approximation that the total detectable height is equal to the detectable height at the center of imaging area. Naturally this height is smaller than the detectable height at the opposite edge of imaging area and small overestimation is done when the most distant voxels are neglected (see figure 2.7 b)). Also for the symmetry of the observation matrix the number of slices in z direction is odd, when the center slice (2D-slice) is at the same height as the center line of the collimator hole.

If r is the radius of collimator hole, h the length of the hole and l the length from the front end of the collimator to the center of imaging area (see Figure 5.2) we can write for the similar triangles in Figure 2.7 a):

$$\frac{2r}{h} = \frac{x}{l+h} \tag{2.24}$$

where x is the maximum detectable height from the "bottom" of collimator hole. Now the visible height s to the other direction is is

$$s = x - \frac{dz}{2}, \tag{2.25}$$

where dz is the voxel width in z direction. The number of planes N_z will be

$$N_z = 1 + 2 \cdot \mathrm{floor}(\frac{s - \frac{dz}{2}}{dz}) \tag{2.26}$$

where floor$(\cdot)$ stands for rounding toward zero. For example with 6P-SPECT the detectable height will be about 3.2 cm at the center of the imaging area and the homogeneity along z-axis proper approximation. With image size of 288×288 mm^2 and 64×64 pixels, the number of slices in z-direction will be 7.

Again we will formulate the constraint matrix form. We aim for a similar ROI matrix as in Section 2.3.2. This ROI matrix operates to the 2D activity distribution vector and results three dimensional activity distribution with no variation in z-direction. If we denote the two-dimensional activity distribution with $f \in \mathbf{R}^{N^2 \times 1}$ and three-dimensional activity distribution with $\eta \in \mathbf{R}^{N_z N^2 \times 1}$, the relation will be:

$$\eta = Bf \tag{2.27}$$

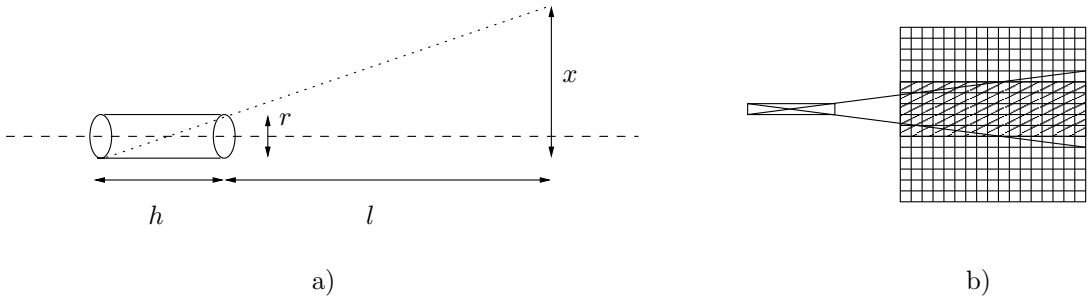

Figure 2.7: Determination of the reconstruction height. a) The similar triangles for determination of x. b) Selected slices in z direction marked with pattern.

Formation of matrix B is easy, we just simply stack N_z pieces of $N^2 \times N^2$ sized unity matrices above each other. Similarity to ROI-model is obvious, we have selected N^2 ROI's in z-direction. Here each ROI has an volume of N_z voxels.

Now the $2\frac{1}{2}$D observation model can be written as

$$P = H\eta + v = HBf + v = \widehat{H}f + v \tag{2.28}$$

This constrain regularizes the fully 3D problem since the number of reconstruction parameters is reduced from $N_z N^2$ to N^2.

Chapter 3

Reconstruction of the activity distribution

In this chapter we consider the theory of the reconstruction of the activity distribution in SPECT. The Fourier-based Filtered Back Projection - technique is shown, although it will not produce accurate images due the low number of projections in 6P-SPECT.

For accurate estimation of the activity distribution some algebraic methods are needed. Both deterministic and statistical approaches for solving the inverse problem in SPECT are considered. Also the regularization of the ill-posed problem is discussed.

The FBP methods are still widely used in clinical applications, since the more advanced methods require more computer time. In 6P-SPECT, however, the number of projections is low and thus the dimensions of the problem are low as well. As a consequence, in the case of 6P-SPECT the time required by the advanced methods (such as least squares or maximum likelihood estimation) is also relatively low, and the use of these methods is preferable.

The dynamical effects, e.g. clearance and physical and biological half-life of the nuclide is not considered in this thesis. By multiple measurements time-activity curves of certain organs could be estimated [7]. Also time-varying reconstruction models can be used to include dynamical effect to estimates [24].

3.1 Filtered Back Projection

The derivation of Filtered Back Projection (FBP) is given in e.g. [22] and [5], we will follow the presentation in the first one. Derivation is done in continuous case and in Section 3.1.3 the computer implementation of the method is discussed. For comparison between FBP and other reconstruction methods see [44].

3.1.1 Radon transform

In the continuous case the formation of projections can be modeled by Radon transform. Radon transform integrates the values of the object function $f(x, y)$ along parallel straight lines. The projection is formed by combining a set of line integrals. With geometry described in Figure 3.1, the Radon transform of f to measurement angle θ can be written with delta function as

$$P_\theta(t) = \int_{-\infty}^{\infty} \int_{-\infty}^{\infty} f(x, y)\delta(x\cos\theta + y\sin\theta - t)dxdy \tag{3.1}$$

3.1.2 Fourier-Slice theorem

The Fourier-Slice theorem connects the one-dimensional Fourier transform of the parallel projection to the two-dimensional Fourier transform of the original object function.

The two-dimensional Fourier transform of the object function $f(x, y)$ in the continuous case is

$$F(u, v) = \int_{-\infty}^{\infty} \int_{-\infty}^{\infty} f(x, y)e^{-j2\pi(ux+vy)}dx\ dy. \tag{3.2}$$

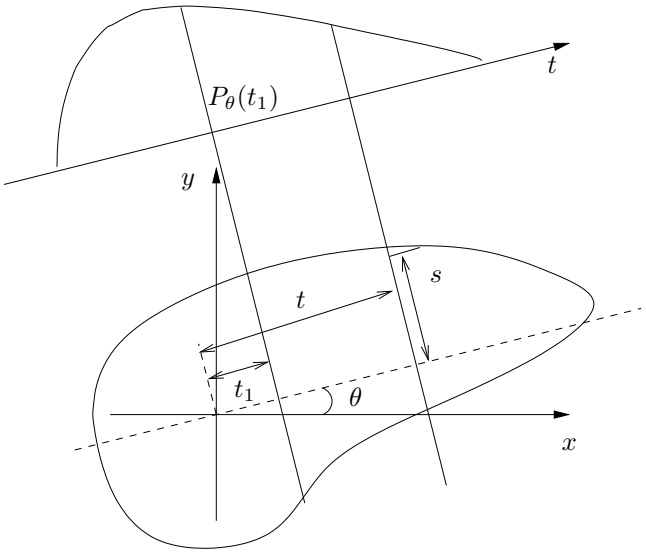

Figure 3.1: Geometry of the Radon transform.

The equation for projection $P_\theta(t)$ can be simplified by selecting a new coordinate system (t, s), which is a rotated version of the (x, y)-coordinate system, that is,

$$\begin{bmatrix} t \\ s \end{bmatrix} = \begin{bmatrix} \cos\theta & \sin\theta \\ -\sin\theta & \cos\theta \end{bmatrix} \begin{bmatrix} x \\ y \end{bmatrix}. \tag{3.3}$$

In this new coordinate system the projection along straight line, that is, over constant t can be written in the form

$$P_\theta(t) = \int_{-\infty}^{\infty} f(t, s)ds \tag{3.4}$$

and the one-dimensional Fourier transform of the projection in (t, s) system is

$$S_\theta(\omega) = \int_{-\infty}^{\infty} P_\theta(t)e^{-j2\omega\pi t}dt. \tag{3.5}$$

By substituting $P_\theta(t)$ by Eq. (3.4) in Eq. (3.5) and transforming the result in back (x, y)-coordinate system by relationships in Eq. (3.3), the Fourier transform of the projection can be written as

$$S_\theta(\omega) = \int_{-\infty}^{\infty}\int_{-\infty}^{\infty} f(x, y)e^{-j2\omega\pi(x\cos\theta+y\sin\theta)}dxdy. \tag{3.6}$$

Eq. (3.6) represents the two-dimensional Fourier transform of the object function at a spatial frequency of $(u = \omega\cos\theta, v = \omega\sin\theta)$ and thus we can write:

$$S_\theta(\omega) = F(\omega, \theta) = F(\omega\cos\theta, \omega\sin\theta) = F(u, v), \tag{3.7}$$

which is the Fourier-Slice theorem.

3.1.3 Derivation of the FBP-method

When the Fourier transform $F(u, v)$ of the object function $f(x, y)$ is known, the object function can be represented by the Inverse Fourier Transform (IFT):

$$f(x, y) = \int_{-\infty}^{\infty}\int_{-\infty}^{\infty} F(u, v)e^{j2\pi(ux+vy)}dudv. \tag{3.8}$$

Next we can replace the rectangular coordinate system (u, v) in the frequency domain with the polar coordinates (ω, θ) using relations

$$u = \omega \cos\theta \tag{3.9}$$
$$v = \omega \sin\theta \tag{3.10}$$
$$dudv = \omega \; d\omega \; d\theta \tag{3.11}$$

The IFT of a polar function is

$$f(x,y) = \int_0^{2\pi} \int_0^{\infty} F(\omega,\theta) e^{2j\pi\omega(x\cos\theta + y\sin\theta)} \omega \; d\omega \; d\theta. \tag{3.12}$$

The integration over 2π, or 360° can be split into two parts, first from 0° to 180 ° and then from 180° to 360°:

$$\begin{aligned} f(x,y) &= \int_0^{\pi} \int_0^{\infty} F(\omega,\theta) e^{2j\pi\omega(x\cos\theta + y\sin\theta)} \omega \; d\omega \; d\theta \\ &\quad + \int_0^{\pi} \int_0^{\infty} F(\omega,\theta+\pi) e^{2j\pi\omega(x\cos(\theta+\pi) + y\sin(\theta+\pi))} \omega \; d\omega \; d\theta. \end{aligned} \tag{3.13}$$

$F(\omega, \theta)$ is periodic function of θ with period π, that is,

$$F(\omega, \theta + \pi) = F(-\omega, \theta). \tag{3.14}$$

Therefore the Eq. (3.13) can be written in the form

$$f(x,y) = \int_0^{\pi} \left[\int_{-\infty}^{\infty} F(\omega,\theta) |\omega| e^{2j\pi\omega t} d\omega \right] d\theta, \tag{3.15}$$

where $t = x\cos\theta + y\sin\theta$. Next the two-dimensional Fourier transform of the object function $F(\omega, \theta)$ can be replaced according to Eq. (3.7) with the projection at angle θ, $S_\theta(\omega)$:

$$f(x,y) = \int_0^{\pi} \left[\int_{-\infty}^{\infty} S_\theta(\omega) |\omega| e^{2j\pi\omega t} d\omega \right] d\theta \tag{3.16}$$

The inner integral of Eq. (3.16) represents filtering of the projection $S_\theta(\omega)$ with a ramp filter. This gives a reason to define a new variable, $Q_\theta(t)$, which is called the *Filtered Projection*:

$$Q_\theta(t) = \int_{-\infty}^{\infty} S_\theta(\omega) |\omega| e^{j2\pi\omega t} d\omega \tag{3.17}$$

To obtain the original object function, the filtered projections at angles θ_i are back-projected using the Eq. (3.16).

About implementation of the FBP-algorithm

There are two different approaches to implement FBP-algorithm in the discrete case. In both approaches first the measured projections are filtered and then filtered projections are back-projected to the image plane. Difference in the methods is in the filtering process which can be done either in frequency or space domain. The fastest and most widely used method uses FFT (Fast Fourier Transform)-algorithm. When this method is used the filtering of the projections is done in frequency domain. In this case the properties of FFT-algorithm must be considered. Since the FFT-algorithm is periodic and the convolution in Eq. (3.17) is aperiodic, one must zero-pad the projection data to reduce the effect of periodic convolution. If the projection is sampled at N points, it must be zero-padded to $(2N-1)$ elements to avoid interperiodic interference. And when base 2 FFT algorithm is used, the projections must be padded to $(2N-1)_2$ elements, the smallest integer that is power of two and lager than $(2N-1)$.

Also the ramp filter needs some modifications in the discrete case. Although the ideal ramp filter with frequency response $|\omega|$ is zero only at frequency $\omega = 0$ (dc component of the projection data), the straightforward discrete implementation of this ramp filter zeros out not only the zero frequency but an finite band of low frequencies. This causes an dc shift in reconstructions and therefore the filter cannot have zero gain for dc component. Also the high-pass ramp filter can amplify the high frequency noise in observation and produce severe artifacts. To avoid this, often an *smoothing window* or a low-pass filter is incorporated to the filtering process. This, in a way, regularizes the FBP-algorithm [5]. Effects of different filtering is discussed in [29]. In general filters that produce higher resolution also augment noise in projection data and lower resolution filters reduce the effect of noise.

When FFT-implementation is used, the filtering process can be written as in [22]:

$$\begin{aligned} Q_\theta(n\tau) \quad = \quad & \tau \times \text{IFFT} \left\{ [\text{FFT } P_\theta(n\tau) \text{with ZP}] \right. \\ & \left. \times [\text{FFT } h(n\tau) \text{with ZP}] \times \text{smoothing window} \right\} \end{aligned} \tag{3.18}$$

where FFT and IFFT stand for fast Fourier transform and inverse fast Fourier transform, τ is the sampling interval of the projections , $h(n\tau)$ is the impulse response of the used filter and ZP stands for zero-padding of the data. The back-projection can be done by discrete approximation of Eq. (3.16):

$$f(x, y) = \frac{\pi}{M} \sum_{k=1}^{M} Q_{\theta_k}(x \cos\theta_k + y \sin\theta_k), \tag{3.19}$$

where the summation is done over the M measurement angles θ_k. Usually the values of $x \cos\theta_k + y \sin\theta_k$ do not correspond to the values of t, the points where the filtered projection Q_θ is defined and some kind of interpolation is needed.

3.1.4 Discrete version of Fourier transform

One-dimensional Inverse Discrete Fourier Transform (IDFT) of vector f is defined as

$$f_m = \sum_{n=0}^{N-1} \hat{f}_n \exp\left(i \frac{2\pi}{N} nm \right). \tag{3.20}$$

In Equation (3.20) f_m is presented as a linear combination of functions $e^{i\frac{2\pi}{N}nm}$. If we denote $\omega = 2\pi/N$, the transform can be written as

$$\begin{pmatrix} f_0 \\ f_1 \\ \vdots \\ f_{N-1} \end{pmatrix} = \begin{pmatrix} 1 & 1 & \dots & 1 \\ 1 & e^{i\omega} & \dots & e^{i(N-1)\omega} \\ 1 & e^{i2\omega} & \dots & e^{i(N-1)2\omega} \\ \vdots & \vdots & & \vdots \\ 1 & e^{i(N-1)\omega} & \dots & e^{i(N-1)(N-1)\omega} \end{pmatrix} \begin{pmatrix} \hat{f}_0 \\ \hat{f}_1 \\ \vdots \\ \hat{f}_{N-1} \end{pmatrix}. \tag{3.21}$$

Thus, the IDFT can be represented with a matrix product

$$f = \Psi \hat{f}, \tag{3.22}$$

in which the general element of Ψ is defined as

$$\Psi_{m,n} = e^{i\omega mn}; \quad \text{where} \quad m, n = 0, 1, \dots, N-1. \tag{3.23}$$

The Inverse Discrete Fourier Transform matrix Ψ has an inverse operator since all of its columns are orthogonal. The inverse matrix which represents the Discrete Fourier Transform will be

$$\Psi^{-1} = \frac{1}{N} \Psi^{\mathrm{T}}. \tag{3.24}$$

3.1.5 Discrete version of FBP

The filtering process described in Eq. (3.17) can be written in the discrete case when we know the frequency response $A(\omega)$ of the desired filter. As known in case of Finite Impulse Respond or FIR-system, the impulse response a of filter described by $A(\omega)$ can be approximated using the Inverse Discrete Fourier Transform:

$$a = \mathrm{IDFT}(A) = \Psi A. \tag{3.25}$$

When the impulse respond a is known, the filtering of signal f is done using convolution which can be written in the form

$$\hat{f}_t = \sum_{l=0}^{N-1} a_l f_{t-l}. \tag{3.26}$$

In the matrix form Eq. (3.26) can be written as

$$\hat{f} = Wf, \tag{3.27}$$

where

$$W = \begin{pmatrix} a_0 & a_1 & a_2 & \cdots & a_{N-1} \\ a_{N-1} & a_0 & a_1 & \cdots & a_{N-2} \\ \vdots & & & & \\ a_1 & a_2 & a_3 & \cdots & a_0 \end{pmatrix}. \tag{3.28}$$

Filtered Back Projection requires that each projection is filtered separately. As described in Section 2.1, $P \in \mathrm{R}^{L \cdot M \times 1}$ is the combined projection vector that consists of M pieces of $(L \times 1)$-sized blocks which each corresponds to projection at one measurement angel. If we form a matrix Ω which is a diagonal block matrix:

$$\Omega = \begin{pmatrix} W & & & & \\ & \ddots & & 0 & \\ & & W & & \\ & 0 & & \ddots & \\ & & & & W \end{pmatrix}, \tag{3.29}$$

the block-by-block filtering can be done by simple matrix multiplication:

$$\hat{P} = \Omega P. \tag{3.30}$$

Filtered projections can be back-projected as in Eq. (3.19) but then some kind of interpolation is needed. If we construct a matrix R that represents the discrete version of Radon transform, FBP algorithm can be written as

$$\hat{f}_{\mathrm{FBP}} = R^{\mathrm{T}} \Omega P, \tag{3.31}$$

where the transpose of Radon transform matrix R^{T} is the back-projection operator. In Eq. (3.30) the filtering of the projections is done separately for each projection angle. Consequently, the dependencies between the projections to different angles are not considered in reconstruction with FBP and therefore some amount of information is lost. For example, the projections to angles with spacing of 180° are most certainly not independent and this information should be incorporated in the reconstruction. The more sophisticated reconstruction methods operate on the combined projection data and the dependencies between the separate projections are included in the reconstruction with the correctly constructed observation model.

3.2 Deterministic methods

Here we will discuss the classical approaches to solving linear ill-posed problems. We are concerned with the least squares estimation in the case of underdeterministic problems. Consequently, the minimum norm estimate and Tikhonov regularization are discussed.

The deterministic approach to the inverse problem in SPECT has some drawbacks. The unregularized minimum norm estimate gives poor results especially with the limited number of projections and as shown in Section 3.3.4, the use of Tikhonov regularization includes implicit assumptions that are not valid in SPECT. In this section we will follow the representation given in [21]. Detailed discussion of several imaging problems including tomography is given in [5] and the fundamentals of the matrix based reconstruction in [34] and [33].

3.2.1 Least-squares estimation

In the least squares estimation the relationship between the observations and the parameters is assumed to be as in Eq. (2.3). The least squares solution $\hat{f}_{\mathrm{LS}}$ minimizes the Euclidean norm of the residual $P - Hf$, that is

$$\hat{f}_{\mathrm{LS}} = \arg\min ||P - Hf||. \tag{3.32}$$

The range $\mathcal{R}$ of matrix H is defined as

$$\mathcal{R}(H) = \left\{ g \in \mathbf{R}^{b\times 1} \mid g = Hf \text{ for some } f \in \mathbf{R}^{N^2\times 1} \right\}, \tag{3.33}$$

and the null space as

$$\mathcal{N}(H) = \left\{ f \in \mathbf{R}^{N^2\times 1} \mid Hf = 0 \right\}. \tag{3.34}$$

The existence of solution requires that $P \in \mathcal{R}(H)$. Furthermore, the solution would be unique only if $\mathcal{N}(H) = \{0\}$, that is, when the null space of the observation matrix H is trivial.

The LS-estimate minimizes also the following index

$$l_{\mathrm{LS}} = ||P - Hf||^2 = (P - Hf)^{\mathrm{T}}(P - Hf). \tag{3.35}$$

The index l_{LS} will be at minimum when the residual belongs to the orthogonal complement of H, that is $P - Hf \in \mathcal{R}(H)^{\perp}$. Because $\mathcal{R}(H)^{\perp} = \mathcal{N}(H^T)$, we get for the minimizing parameter of Eq. (3.35) the following characterization:

$$H^{\mathrm{T}}(P - Hf) = 0. \tag{3.36}$$

Equation (3.36) equals to

$$H^{\mathrm{T}}P = H^{\mathrm{T}}Hf. \tag{3.37}$$

Now if $\mathcal{N}(H^{\mathrm{T}}) = \{0\}$, the LS-solution is unique and we can write

$$\hat{f}_{\mathrm{LS}} = (H^{\mathrm{T}}H)^{-1}H^{\mathrm{T}}P. \tag{3.38}$$

Thus, this is the overdeterministic case when the number of observations is greater than the number of parameters to be estimated. However, in SPECT the model is underdeterministic and $\mathcal{N}(H^{\mathrm{T}}) \neq \{0\}$ and $\mathcal{N}(H) \neq \{0\}$, so the inverse of $H^{\mathrm{T}}H$ can not be found. This means that there are several solutions for equation (3.36) and one must choose one of them. One widely used estimate is minimum norm solution $\hat{f}_{\mathrm{MN}}$, the solution whose Euclidean norm is at minimum. $\hat{f}_{\mathrm{MN}}$ is defined as

$$\hat{f}_{\mathrm{MN}} = H^{\dagger}P = \arg\min \left\{ ||\hat{f}_{\mathrm{LS}}|| \mid \hat{f}_{\mathrm{LS}} = \arg\min ||P - Hf|| \right\}, \tag{3.39}$$

where $H^{\dagger}$ stands for *pseudoinverse* or *generalized inverse* of H. Reconstruction with generalized inverses is discussed in [47]. If the Rank(H) equals to the number of observations and the model is underdeterministic, the pseudoinverse can be written in the form

$$H^{\dagger} = H^{\mathrm{T}}\left(HH^{\mathrm{T}}\right)^{-1}. \tag{3.40}$$

The selection of minimum norm has usually no physical motivation. The Euclidean norm of the real activity distribution f should not be small since it's obvious that $f_i \geq 0 \ \forall \ i$. Since the active elements of f have large values, minimum norm solution produces strongly negative artifacts in reconstructed f to keep the norm of the solution small and therefore does not give acceptable solutions.

3.2.2 Tikhonov regularization

Since the inverse problem in SPECT is *ill-posed*, we need to modify the problem to get the solution stable. An ill-posed problem has properties that cause small errors in measurement data to cause large errors in estimate. One way to modify the LS-problem (3.32) is the generalized Tikhonov regularization:

$$\hat{f}_\alpha = \arg\min \left\{ ||P - Hf||^2 + \alpha ||L(f - f_*)||^2 \right\}. \tag{3.41}$$

Here α is the regularization parameter and $||L(f - f_*)||$ is the so called side constraint. In generalized Tikhonov regularization α controls the weighting of the side constraint compared to the residual in the minimization process.

Common way to choose the side constraint is to set $f_* = 0$ and include the prior information of solution f to L. If solution f is know to be smooth, the we could choose the matrix L to be first or second difference matrix. During reconstruction in SPECT the two-dimensional activity distribution will be given with 1D vector so the difference matrices must be modified to satisfy the 2D smoothness. Because of indexes of neighboring pixels in 2D figure and 1D vector will not be same, the normal difference matrices can not be used in L. We will not discuss the smoothness priors here since with TRT the activity distribution can also be point-like and the use of smoothness priors is not reasoned.

The other choice for L is the identity matrix I. With this constraint and $f_* = 0$, the problem in Eq. (3.41) will reduce to

$$\hat{f}_\alpha = \arg\min \left\{ ||P - Hf||^2 + \alpha ||f||^2 \right\}. \tag{3.42}$$

Clearly this leads to solution, where the norm of the parameter vector f will be small, depending on α. Solution of equation (3.42) is called the *standard Tikhonov regularized solution.*

The Equation (3.41) can be modified to solution of LS-problem

$$\hat{f}_\alpha = \arg\min \left\{ ||\widetilde{P} - \widetilde{H}f||^2 \right\}, \tag{3.43}$$

where

$$\widetilde{H} = \begin{pmatrix} H \\ \sqrt{\alpha}L \end{pmatrix}, \quad \widetilde{P} = \begin{pmatrix} P \\ \sqrt{\alpha}Lf_* \end{pmatrix}. \tag{3.44}$$

For $\widetilde{H}$ the inverse of $\widetilde{H}^{\mathrm{T}}\widetilde{H}$ can always be found and the solution for regularized problem can be calculated as in Eq. (3.38)

$$\hat{f}_\alpha = \left(\widetilde{H}^{\mathrm{T}}\widetilde{H} \right)^{-1} \widetilde{H}^{\mathrm{T}}\widetilde{P}. \tag{3.45}$$

In Section 3.3.4 will be shown that the use of Tikhonov regularization includes some implicit statistical assumptions that are not desirable in SPECT. Since the calculation of the matrix inverse in Equations (3.45), (3.40) and (3.38) is time consuming, especially when the dimensions of the model increase, the LS and Tikhonov estimates are calculated by some iterative methods, for example Conjugate-Gradient (CG) method [49]. The Conjugate-Gradient method converges to the minimum norm solution and the number of iterations can be used as regularization [44].

3.3 Statistical inversion theory, Bayesian estimation

In statistical inversion theory both observations P and estimated parameters f are considered to be random variables with joint distribution $p(f, P)$. The goal in Bayesian estimation is to construct a model for the probability distribution of the estimation parameters with condition, that the observations are fixed. This is achieved by incorporating the prior information of the estimation parameters to the statistical model, that describes the formation of the observations.

3.3.1 Posterior density

For radioactive decay, if f is the activity of the isotope in some region of the imaging area, the number of emissions from that area is a random variable A. If we denote the probability density function of A with $p(A)$, and approximate the density with Poisson-distribution function, we get for the probability density

$$p(A) = e^{-f}\frac{f^A}{A!}. \tag{3.46}$$

The model for formation of projection at projection bin p_i will be

$$p_i = \sum_{j=1}^{N} H_{ij}A_{ij} + v_i, \tag{3.47}$$

where $A_{ij} \sim \text{Poisson}(f_j)$, v_i is the additive Gaussian noise and H_{ij} the elements of the observation matrix described in Section 2. If the measurement error v_i is neglected, the projection p_i will also be Poisson distributed variable, that is $p_i \sim \text{Poisson}(\sum_{j=1}^{N} H_{ij}f_j)$. With that approximation the posterior density of p_i is

$$p(p_i|f) = \mathrm{e}^{-\sum_{j=1}^{N} H_{ij}f_j}\frac{(\sum_{j=1}^{N} H_{ij}f_j)^{p_i}}{p_i!}, \tag{3.48}$$

and for the posterior density of P we can write

$$p(P|f) = \prod_{i=1}^{b} \mathrm{e}^{-\sum_{j=1}^{N} H_{ij}f_j}\frac{(\sum_{j=1}^{N} H_{ij}f_j)^{p_i}}{p_i!}. \tag{3.49}$$

Next we will use Bayes' equation which allows us to construct the posterior density function $p(f|P)$ which is formally the solution of the inverse problem. The Bayes' equation is

$$p(f, P) = p(f|P)p(P) = p(P|f)p(f), \tag{3.50}$$

where $p(P|f)$ is called the likelihood function and $p(f)$ is called the prior density of f. Since the measured values are known, that is, the values of P are fixed, the prior density $p(P)$ is constant. So the posterior density of f is

$$p(f|P) \propto p(P|f)p(f). \tag{3.51}$$

3.3.2 Point estimates $\hat{f}_{\text{MAP}}$ and $\hat{f}_{\text{ML}}$

Although the posterior density is formally the solution of the inverse problem, it is function of several variables and does not yet give the information in which we are interested. To obtain a concrete solution one must calculate a point estimate, that is, to solve some parameters of the posterior density. One common point estimate is *Maximum a posteriori*-estimate, the maximum point of posterior density.

$$\hat{f}_{\text{MAP}} = \arg\max p(f|P). \tag{3.52}$$

When Bayesian estimation is used the selection of prior density $p(f)$ plays an important role. The prior density of f should include all the information of the solution that is available before the measurements. For example with emission tomography, we can not assume any smoothness priors, actually only true prior is the non-negativity of the solution f, that is

$$p_+(f) = \begin{cases} 1, & f_k \geq 0 \ \forall\, k \\ 0, & \text{otherwise} \end{cases}. \tag{3.53}$$

The use of too strong priors can lead to a situation, when the approximation:

$$p(f|P) = p(P|f)p(f) \sim p(f) \tag{3.54}$$

can be done and formally the measurements do not affect the solution.

We will use a point estimate called maximum likelihood, that simply maximizes the likelihood $p(P|f)$, without concerning the prior density of f.

$$\hat{f}_{\mathrm{ML}} = \arg\max p(P|f) \tag{3.55}$$

In other words, f_{ML} is the solution that would most probably produce the observation P. For inverse problems this corresponds to the non-regularized problem and should not by itself produce reasonable reconstructions. However, in calculation of the ML-estimate we use the Maximum Likelihood Expectation Maximization-algorithm. This algorithm includes a implicit non-negativity constrain and it regularizes the problem.

3.3.3 ML-EM algorithm

We will derive the ML-EM algorithm for Emission Tomography as in [32]. Alternative derivation of ML-EM algorithm is given in [45]. Modifications of EM-algorithm can be used to include concave priors in iteration [41] or to calculate Maximum a Posteriori-estimate [16]. Alternative approach in PET is shown in [51], where instead of maximizing the likelihood, the equal point estimate is achieved by the minimization of cross-entropy.

Calculation of ML-estimate requires much more memory and computer time than FBP-based estimates and therefore it is not yet in clinical use. There are some studies of implementing the ML-EM iteration process on multiple computers and even a WWW-interface of parallel computers for routine use [20, 13].

Because the maximization of the likelihood in Eq. (3.49) is difficult, maximization will be done with so called *complete data* z_{ij}, the number of photons emitted from pixel j and detected at projection bin i. Clearly $z_{ij} = H_{ij}A_{ij}$ and $z_{ij} \sim \mathrm{Poisson}(H_{ij}f_j)$. If we now write the complete data in one vector z, the posterior density will be

$$p(z|f) = \prod_{i=1}^{b}\prod_{j=1}^{N} \mathrm{e}^{-H_{ij}f_j}\frac{(H_{ij}f_j)^{z_{ij}}}{z_{ij}!} \tag{3.56}$$

In each iteration there are two steps: first the conditional expectation $E\{\ln p(z|f)\big|P, \hat{f}^{(n)}\}$ is calculated and after this the maximization of the conditional expectation is done with respect to f, while $\hat{f}^{(n)}$ is held fixed. The new parameter estimates $\hat{f}^{(n+1)}$ are obtained from the maximizing parameters. The logarithm of $p(z|f)$ is

$$\ln p(z|f) = \sum_{i=1}^{b}\sum_{j=1}^{N}(-H_{ij}f_j + z_{ij}\ln(H_{ij}f_j) - \ln(z_{ij}!)). \tag{3.57}$$

The conditional expectation of $\ln p(z|f)$ with respect to the measurement data P and the current estimate $\hat{f}^{(n)}$ will be

$$E\left\{\ln p(z|f)\big|P, \hat{f}^{(n)}\right\} = \sum_{i=1}^{b}\sum_{j=1}^{N}(-H_{ij}f_j + N_{ij}\ln(H_{ij}f_j)) + R, \tag{3.58}$$

where R does not depend on the new f and N_{ij} stands for the conditional expectation of z_{ij}:

$$N_{ij} = E\left\{z_{ij}\big|p_i, \hat{f}^{(n)}\right\} = \frac{H_{ij}\hat{f}_j^{(n)}p_i}{\sum_{k=1}^{N}H_{ik}\hat{f}_k^{(n)}} \tag{3.59}$$

The following step is to calculate the maximum of the conditional expectation obtained in Eq. (3.58). This is relatively simple task since $E\{\ln p(z|f)\big|P, \hat{f}^{(n)}\}$ is concave in f [32] and the maximum can be found by setting the partial derivatives equal to zero:

$$\frac{\partial}{\partial f_j}\left(E\left\{\ln p(z|f)\big|P, \hat{f}^{(n)}\right\}\right) = 0 \tag{3.60}$$

$$\frac{\partial}{\partial f_j}\left(\sum_{i=1}^{b}\sum_{j=1}^{N}(-H_{ij}f_j + N_{ij}\ln(H_{ij}f_j)) + R\right) = 0, \tag{3.61}$$

which leads to

$$-\sum_{i=1}^{b} H_{ij} + \sum_{i=1}^{b} N_{ij}\frac{1}{f_j} = 0. \tag{3.62}$$

Now combining the Equations (3.59) and (3.62), the iteration formula for ML-EM solution becomes

$$\hat{f}_j^{(n+1)} = \frac{\sum_{i=1}^{b} N_{ij}}{\sum_{i=1}^{b} H_{ij}} = \frac{\hat{f}_j^{(n)}}{\sum_{i=1}^{b} H_{ij}}\sum_{i=1}^{b}\frac{H_{ij}p_i}{\sum_{k=1}^{N} H_{ik}\hat{f}_k^{(n)}} \tag{3.63}$$

There are two remarkable advantages in use of ML-EM-algorithm. First, in every iteration the expected number of photons is equal to the total number of observed photons, that is $\sum_{i=1}^{b} H_{ij}f_j = \sum_{i=1}^{b} p_i$. Second, when the initial guess for parameters f is positive, then at every iteration the solution is non-negative. This equals formally to the $\hat{f}_{\mathrm{MAP}}$-estimate with prior density equal to Eq. (3.53).

In this thesis we consider the attenuation distribution of the target as prior information, that is, we assume that the attenuation map is measured with for example CT-scan before the construction of the observation matrix. However, methods for simultaneous estimation of both the attenuation and the activity distributions using plain projection data are presented in the literature. In the 6P-SPECT the low number of projections makes the simultaneous estimation difficult and therefore it was not considered. So called Intra-SPECT approaches to simultaneous activity and attenuation reconstruction with Tikhonov and ML approach are given in [11] and [27], respectively.

3.3.4 Tikhonov regularization and normally distributed data

There is a link between the generalized Tikhonov regularization and statistical inversion theory. Here it is used to show the statistical assumptions that are done when generalized form of Tikhonov regularization is used. If the both parameters $f \in \mathbf{R}^N$ and measurement errors $v \in \mathbf{R}^M$ are independent and normally distributed with covariances Γ_f and Γ_v and with expected values f_* and v_*, respectively , we can write for the prior densities:

$$p_f(f) = \frac{1}{(2\pi)^{N/2}|\Gamma_f|^{1/2}}\exp\left(-\frac{1}{2}(f-f_*)^{\mathrm{T}}\Gamma_f^{-1}(f-f_*)\right) \tag{3.64}$$

$$p_v(v) = \frac{1}{(2\pi)^{M/2}|\Gamma_v|^{1/2}}\exp\left(-\frac{1}{2}(v-v_*)^{\mathrm{T}}\Gamma_v^{-1}(v-v_*)\right). \tag{3.65}$$

Now both Hf and $Hf+v$ will both be normally distributed and we can write the posterior density $p(f|P)$ in the following form using Bayes' equation:

$$\begin{aligned} p(f|P) &\propto p(P|f)p_f(f) = p_v(P-Hf)p_f(f) \\ &\propto \exp\left(-\tfrac{1}{2}(P-Hf-v_*)^{\mathrm{T}}\Gamma_v^{-1}(P-Hf-v_*)\right) \\ &\quad \exp\left(-\tfrac{1}{2}(f-f_*)^{\mathrm{T}}\Gamma_f^{-1}(f-f_*)\right) \\ &= \exp\left(-\tfrac{1}{2}Q(f)\right). \end{aligned} \tag{3.66}$$

Because of the symmetry of the normal distribution, the expected value of the posterior density is the maximum point of the distribution, thus we can write

$$\hat{f} = \arg\max p(f|P) = \arg\min Q(f). \tag{3.67}$$

If we set $L_f^{\mathrm{T}} L_f = \Gamma_f^{-1}$ and similar for L_v, where L_i are the Cholesky factors of Γ_i^{-1}, then the minimization of $Q(f)$ is equal to

$$\hat{f} = \arg\min \Big\{ (L_v(Hf - P - v_*))^{\mathrm{T}} (L_v(Hf - P - v_*)) + (L_f(f - f_*))^{\mathrm{T}} (L_f(f - f_*)) \Big\}, \tag{3.68}$$

which can be reshaped to the following form:

$$\hat{f} = \arg\min \left\{ \left\| \begin{pmatrix} L_v H \\ L_f \end{pmatrix} f - \begin{pmatrix} L_v(P - v_*) \\ L_f f_* \end{pmatrix} \right\| \right\}. \tag{3.69}$$

Similarity of the minimization problem in Eq. (3.69) to Eq. (3.43), the generalized Tikhonov regularization, is obvious. This means that formally Tikhonov regularization is equal to LS-estimate with assumption that parameters are normally distributed. Especially when $L = I$, the following implicit assumptions are made:

- Vector elements in f are statistically independent with mean value f_* and moreover the variances of the elements are equal
- Elements of measurement error vector v are also statistically independent with mean value $v_* = 0$ and elements have equal variances (error is equally distributed in the observations).

Since parameters are Poisson-distributed in SPECT, the use of Tikhonov regularization is not reasonable. Also the variances of the elements in f are not equal but depend on the activity of the pixel (number of emitted photons).

Chapter 4

Absorbed dose

In this chapter we will discuss the methods for calculating the absorbed dose to tissue based on the reconstructed activity distribution inside the target. The accurate calculation of the dose distribution based on the known activity distribution is time consuming. It should also be noticed, that the reconstruction of activity distribution is an inverse problem, but the dose distribution can be calculated straightforwardly. The calculated dose distribution can be calibrated using single surface measurement. The calibration requires determination of *surface dose correction coefficient* of the applied nuclide. With this coefficient the lack of scatter at the surface of the object can be taken into account.

The methods that are considered in the following sections are valid only for photon radiation. The β^- radiation can be approximated to have range less than one pixel in reconstructions. We, therefore, do not consider the the contribution of the electrons to the total dose since the calibration of the dose distribution is based solely on the photons.

The photons emitted from therapeutic nuclides have long range and their contribution to the total dose must be calculated as superposition. Also convolution based kernel methods are given for the dose calculation in homogeneous medium [14]. Although normally the inhomogeneity of tissues is not considered in the brachytherapy and in the radionuclide therapy, it can be included to the dose calculation by a correction factor. We will use *effective attenuation coefficient* method that is used mainly in external beam radiation therapy. This method does not take into account the different scatter conditions in the neighborhood of inhomogeneities compared to homogeneous medium. Also the effects of physical and biological half-life of the nuclides are not considered in the dose calculation.

4.1 Absorbed dose and exposure

Here we will consider only the necessary basics of radiological physics. For more information about dosimetry see [1, 31, 30, 35] or [19].

The *energy imparted* ϵ is a stochastic quantity that describes the amount of energy from ionizing radiation that remains in matter of a finite volume V and a mass m. The *absorbed dose* inside the volume V is defined as

$$D = \frac{d\epsilon}{dm}, \tag{4.1}$$

where ϵ is now the expectation value of energy imparted.

The exposure X is defined as

$$X = \frac{dQ}{dm}, \tag{4.2}$$

where dQ is the total charge of the ions released by the photons in the air and that is stopped inside the volume V.

When the number, and also the distributions of charge and direction of propagation, of the electrons entering and leaving the volume V are equal, the state is called *charged particle equilibrium*

(CPE). In the case of CPE the absorbed dose in the air is directly proportional to the exposure:

$$D_{\text{air}} = X \left(\frac{\overline{W}}{e} \right)_{\text{air}}, \tag{4.3}$$

where $\overline{W}_{\text{air}}$ is the mean energy expended in air per ion pair formed. $\overline{W}$ is constant for each gas, independent of the photon energy above few keV. Although the CPE is never precisely satisfied, for example due to the inverse square law of radiation intensity, it can be approximated when the distance from the point source is large.

The *exposure rate constant* Γ_δ $\left[\text{R m}^2\text{Ci}^{-1}\text{h}^{-1}\right]$ of a point source of the activity A at the distance l in the vacuum can be expressed as

$$\Gamma_\delta = \frac{l^2}{A} \left(\frac{dX}{dt} \right). \tag{4.4}$$

This quantity is defined for each nuclide and it replaces the *specific exposure rate constant*. Γ_δ takes into account the exposure rate due to the γ-rays, the characteristic x-rays and the internal bremsstrahlung [1].

The absorbed dose produced by a point source of activity A in the scattering medium, for example in water, at the distance r can be calculated using equation

$$D = Ak\Gamma_\delta \frac{S(r)}{r^2}, \tag{4.5}$$

where k converts the exposure in the air (or the air kerma) to the absorbed dose in the water. $S(r)$ is the MIRD scatter and absorption factor that can be approximated by the Meisberger's scatter and absorption function in the water:

$$S(r) = q_1 + q_2 r + q_3 r^2 + q_4 r^3, \tag{4.6}$$

where q_i:s are defined empirically for each nuclide.

TABLE 4.1: Conversion factors k for different nuclides and different mediums. k or $(\frac{\mu}{\rho})^{\text{med}}_{\text{air}}$ relates absorbed dose to air kerma.

Nuclide	Mean photon energy (MeV)	k		
		Water	Bone	Muscle
^{192}Ir	0.370	1.112	1.072	1.102
^{60}Co	1.25	1.112	1.062	1.102
^{125}I	0.028	1.013	4.850	1.0516

TABLE 4.2: Coefficients for Meisberger's scatter and absorption function in water for different nuclides.

Nuclide	q_0	q_1 [cm^{-1}]	q_2 [cm^{-2}]	q_3 [cm^{-3}]
^{192}Ir	$1.0128 \cdot 10^{9}$	$5.019 \cdot 10^{-3}$	$-1.178 \cdot 10^{-3}$	$-2.008 \cdot 10^{-5}$
^{60}Co	$9.9423 \cdot 10^{-1}$	$-5.318 \cdot 10^{-3}$	$-2.610 \cdot 10^{-2}$	$1.327 \cdot 10^{-4}$
^{137}Cs	1.0091	$-9.015 \cdot 10^{-3}$	$-3.459 \cdot 10^{-4}$	$-2.817 \cdot 10^{-5}$
^{226}Ra	1.0005	$-4.423 \cdot 10^{-3}$	$-1.707 \cdot 10^{-3}$	$7.448 \cdot 10^{-5}$
^{198}Au	1.0306	$-8.134 \cdot 10^{-3}$	$1.111 \cdot 10^{-3}$	$-1.597 \cdot 10^{-4}$

4.2 Surface dose measurement

As shown in [28] the calculated dose can be calibrated by single surface dose measurement. When dose is measured from a surface of scattering medium, there is a lack of scatter from outer side. If the dose in the surface is calculated as in Eq. (4.5), it is overestimated and therefore the calculated dose at the surface must be corrected by a *surface dose correction coefficient* $SDCC(r)$. $SDCC(r)$ is defined as the relation between the measured dose at the surface D_m and the calculated dose D_c in the air at the same point:

$$SDCC(r) = \frac{D_m}{D_c}. \tag{4.7}$$

A third order polynomial was suggested to model $SDCC(r)$ since it has clear analogies with Meisberger's $S(r)$ factor. The $SDCC(r)$ must be determined for each nuclide individually.

If we look at the reconstructed pixel map with relative activities $A_{k,l}$, the relative dose in air at the same point where D_m is measured can be calculated as

$$D_c = \sum_{k,l} \frac{A_{k,l}\Gamma}{r_{k,l}^2}, \tag{4.8}$$

where summation is done over all point-sources (pixels) in image area. $A_{k,l}$ are the relative pixel activities in image area and $r_{k,l}$ the distances from pixel (k,l) to the measurement point. The measured dose at phantom surface is equal to

$$D_m = \sum_{k,l} SDCC(r_{k,l}) \frac{A_{k,l}\Gamma}{r_{k,l}^2} CF_c. \tag{4.9}$$

CF_c is calibration factor that transfers relative dose to absolute dose with respect to measured value D_m.

When $SDCC(r)$ values of a nuclide are known, CF_c can be determined and used to calibrate the relative distribution calculated with Equation (4.5), or attenuation corrected dose distribution, to absolute dose.

TABLE 4.3: $SDCC(r)$ 3rd order polynomial coefficients in water between 2 and 20 cm for different nuclides. Values are obtained from [28].

Nuclide	q_0	q_1 $[\mathrm{cm}^{-1}] \cdot 10^{-1}$	q_2 $[\mathrm{cm}^{-2}] \cdot 10^{-2}$	q_3 $[\mathrm{cm}^{-3}] \cdot 10^{-3}$
^{99m}Tc	0.60	-0.064	-0.20	0.059
^{131}I	0.73	-0.16	-0.094	0.025
^{18}F	0.59	-0.071	-0.18	0.051

4.3 Attenuation correction

The Equation (4.5) includes already homogeneous attenuation correction since the Meisberger's $S(r)$ polynomial is the combined attenuation and scatter function in water. If the target is inhomogeneous, the attenuation must be modeled to obtain reliable results. Especially if inhomogeneities are located between the point of surface dose measurement and the active area of the target, the inhomogeneity correction is necessary.

Inhomogeneous attenuation can be taken account using so called *effective attenuation coefficient method* [19, 30]. Simplified case of inhomogeneous phantom is shown in Figure 4.1. First we can define *effective distance* r' by replacing the inhomogeneity layer of width h with corresponding amount of water:

$$r' = r - h(1 - \rho'), \tag{4.10}$$

where ρ' is density of the inhomogeneity layer and r the normal distance. When the image area is discretized by pixels, the Equation for effective distance will be

$$r'_{i,j} = r - \sum_m h_m(1 - \rho_m), \tag{4.11}$$

where m is the index set of the pixels that a straight line from point source A at pixel (k, l) to point p at pixel (i, j) intersects, h_m the length of intersection in pixel m and ρ_m the density of the m^{th} pixel.

The correction factors for point source A, that are the relations between dose in phantom with inhomogeneities and dose in homogeneous water phantom, are

$$CF_{i,j}^{k,l} = e^{\mu(r - r'_{i,j})}, \tag{4.12}$$

where μ is the linear attenuation coefficient in water. Equation (4.12) describes an *correction matrix* which can be used to calculate the dose in the inhomogeneous medium.

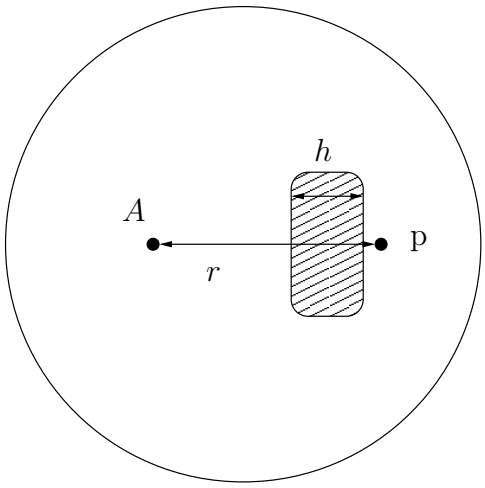

Figure 4.1: Determination of effective distance

4.3.1 Calculation of the attenuation corrected dose

We use a simplified kernel-model in dose calculation. First a normalized *point source kernel*, that describes the dose distribution from a single point-source according to Eq. (4.5), is calculated in homogeneous water phantom. For the attenuation correction a *correction matrix* is calculated for each pixel in image area. In practice the correction matrix must be calculated for all pixels in image area with respect for all point sources (active pixels). Kernel is calculated in a larger grid than actual image size since same kernel is used for all image pixels and it must contain dose distribution to at least to distance of $\sqrt{2}$N pixels.

The dose calculation can be written formally as:

calculate normalized point-source kernel K as in Eq. (4.5) in larger grid that image area
for all (k, l)
  calculate correction matrix $CF^{k,l}$
  match coordinates between K and CF and crop K to size of $N \times N$
  Update the dose distribution: $D_{inh} = D_{inh} + A_{k,l} \cdot K \odot CF^{k,l}$

Example of the attenuation correction is shown in Figure 4.2. The effective attenuation coefficient method does not take into account variation of scatter when density of medium alters. Therefore the boundary effects of the inhomogeneous areas are not modeled in this method.

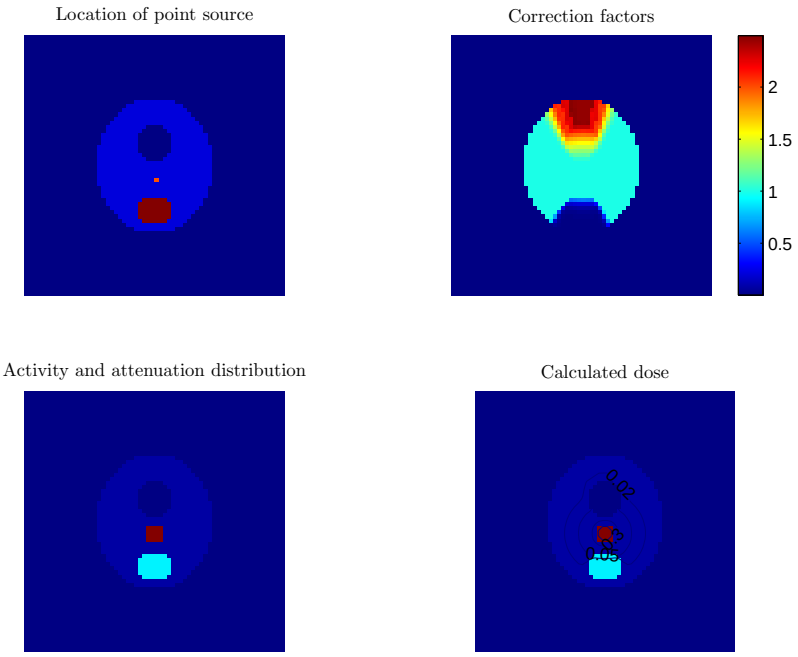

Figure 4.2: Attenuation corrected absorbed dose. At top left is shown attenuation distribution and the place of point source. At top right are the correction factors for point source in previous image. At bottom left is shown the attenuation and activity distribution and at right the attenuation corrected isodoses.

4.4 Limitations of the dose calculation

The described dose calculation methods have some drawbacks. First of all, only 2D distribution is taken into account when dose is calculated. Especially in our phantom studies, when linear iridium sources were used, the source should not be considered as a point in reconstructed plane. The properties of linear source can be taken into account by integrating the activity of the source over the length of the wire and incorporating filtration of the source sealing in the calculation. This leads to integral that can not be evaluated analytically [19]:

$$D(h) = \frac{\Gamma\rho}{h} k \int_{\theta_1}^{\theta_2} e^{-\mu d/\cos\theta} \mathrm{d}\theta, \tag{4.13}$$

where ρ is the linear activity density, μ the linear attenuation coefficient of the filtration of thickness d, h distance of the calculation point from the source and θ_1, θ_2 the angles to the ends of source wire from the calculation point. The exponential term in the Eq. (4.13) represents the filtration in the surface the sealed source. The effect of linearity is largest near the source. We did not take account the linearity since in the near field other effects make the accurate dose calculation difficult.

Because of the limitation in the resolution of the reconstructed activity distribution, the calculated dose is too large near sources. In Section 5.4, results from the measurements with the Lucite phantom show that dose is highly overestimated in the near field (less than 2 cm). This is due to the spread of images of the point sources. Since the resolution of the imaging system is at highest 3.2 mm, the reconstruction of point source will be nearly a bell-curve. This causes artifacts in the calculated dose distribution since the activity reconstruction fails near the point sources. Because the dose is integrated over all active areas in object, the smooth activity distribution overestimates the dose compared to impulse-like activity distribution of a point source. The effect of resolution is not so important when imaging true distributions of radiopharmaceuticals. In real cases the

distributions will be smooth due to the diffusion of the active molecules and also some kind of background activity is present at all times.

The scatter effects of the inhomogeneities are not considered. The Meisberger's polynomials for scatter and attenuation are measured for phantoms, in which dimensions satisfy fully three-dimensional scatter conditions. Inhomogeneities alter the uniform scatter conditions and without modeling in dose calculation it causes errors.

Chapter 5

Simulations and phantom studies

In this Chapter the reconstruction methods are evaluated using simulation and phantom measurements. In addition to the reconstruction of the activity distribution, the dose calculation is verified with measurements using Lucite phantom for simultaneous dose profile and activity projection measurements. All measurements are carried out using 6P-SPECT collimators and a single scintillation crystal as the radiation detector.

5.1 Measurement system

Projections were measured by scanning a scintillation crystal along 6P-SPECT collimator bank. Scintillation crystal was chosen as the radiation detector to achieve better sensitivity than with TLDs (see Section 1.4.2). Scintillation crystal gives also an possibility to reduce the scatter in observations by measuring only photons with certain energy. The rotation of detector system around the object was replaced with rotation of object with respect to collimator. Two different types of phantoms are used, a water tank with linear sources for reconstruction of the activity distribution and a Lucite phantom for dose calculation.

5.1.1 Collimator system and mounting of the phantom and the detector

6P-SPECT measurement system was developed for simultaneous measurement of all projections. This is achieved by placing six one-row collimators around the object. The dimensions of the 6P-SPECT system were designed to satisfy clinical needs: the length of one collimator is 28.8 cm which gives imaging aperture of 50 cm for imaging adult patients and reconstructed image area with the diameter of 25 cm for imaging large organs (Figure 5.2). The radius of collimator holes was $r = 2.5$ mm and length was $h = 8$ cm. The spacing between holes was 2 mm.

Table 5.1: Collimator properties

Dimensions of one collimator bank	
Length	288.0 mm
Width	80.0 mm
Height	20.0 mm
Length of the hole	80.0 mm
Radius of the hole	2.5 mm
Septal thickness	2.0 mm

Since the measurements were made by scanning the collimator holes, we used only one of the six collimators and replaced the collimator rotation, or several collimators at different angles, by phantom rotation. This was achieved by mounting one of the collimators to a board at a fixed position and setting the phantom over a rotating disk attached at the (virtual) center of rotation (see Figures 5.4 and 5.1). This method gives also possibility to measure the projections in

arbitrary angles. The shielded detector (Fig. 5.4) and the was slid along the collimator to measure all projection pixels and then the disk with phantom was rotated. This was repeated until the required number of projections were measured.

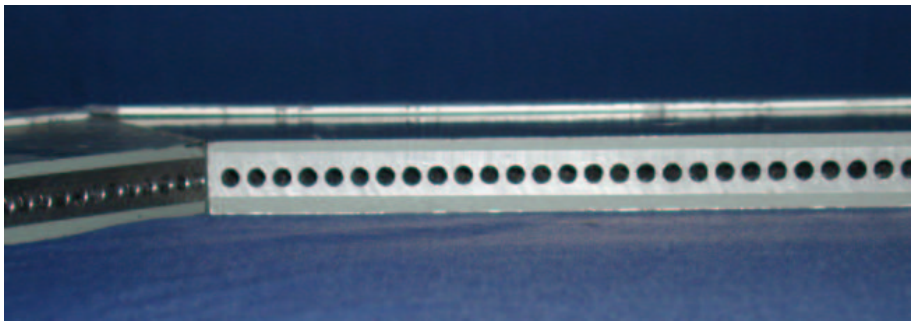

Figure 5.1: Diameter of collimator holes is 0.5 cm.

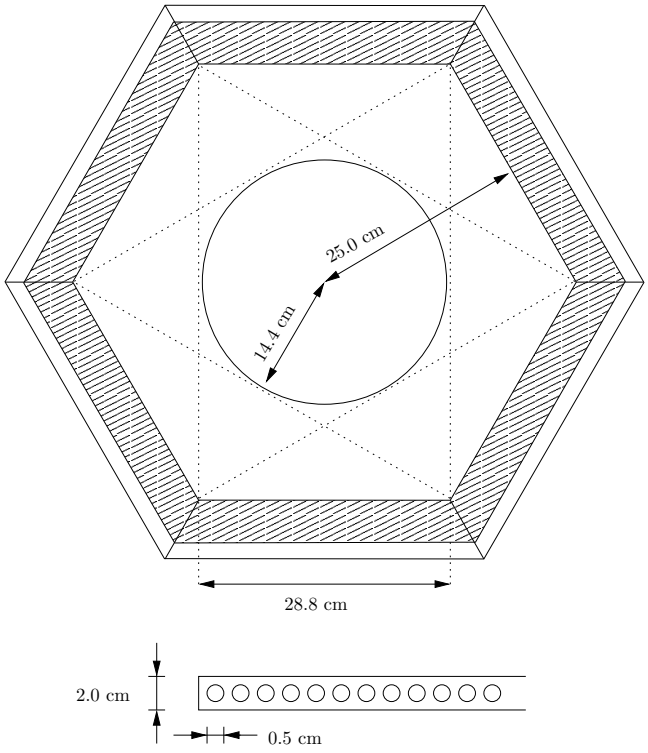

Figure 5.2: Dimensions of 6P-SPECT when collimators are placed in hexagonal form.

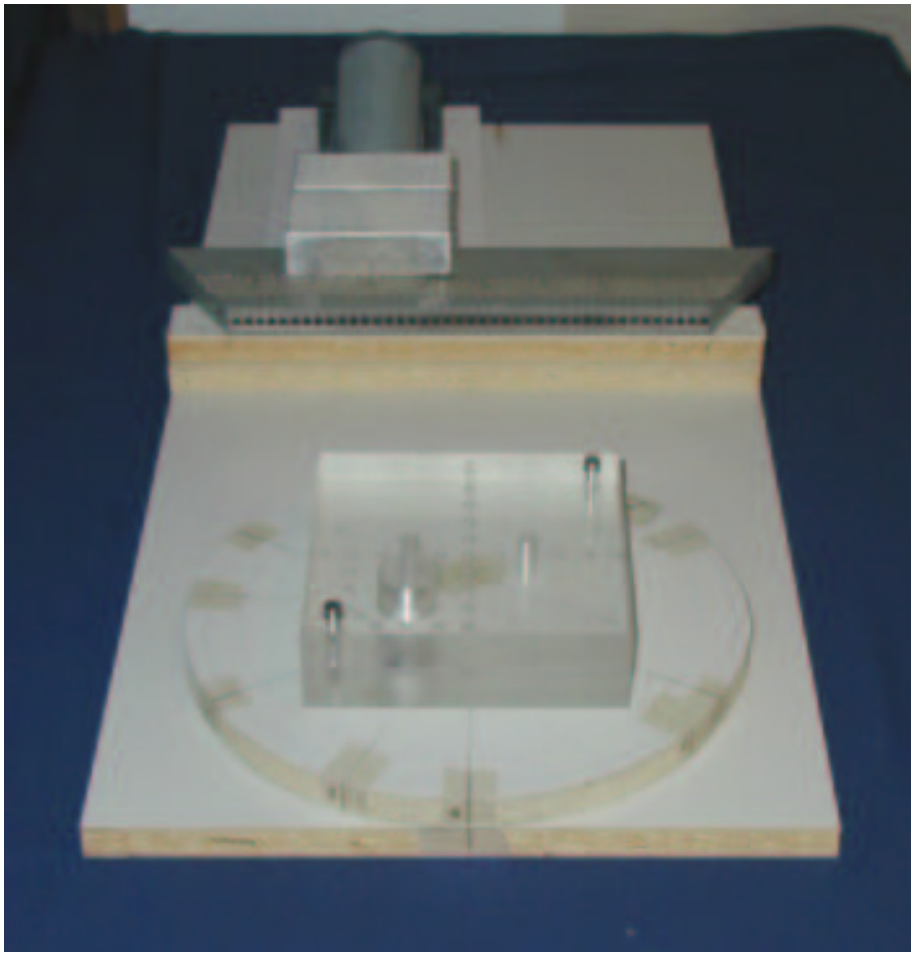

Figure 5.3: Field of view in 6P-SPECT is 28 cm wide. Detectable height at the center of rotation is 1.5 cm from the central plane.

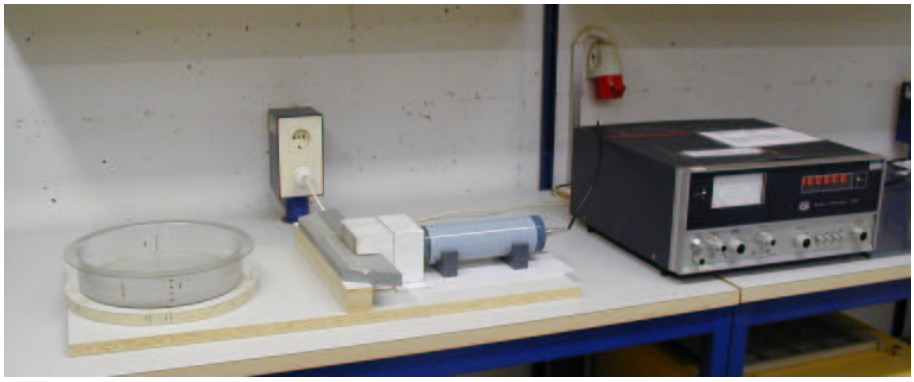

Figure 5.4: Measurement arrangement for phantom studies. Sources were placed inside the water tank which was then rotated to measure projections

5.1.2 ^{192}Ir source

All of the measurements were carried out with ^{192}Ir wire sources used in brachytherapy. ^{192}Ir sources were used because of the good availability and minimal contamination risk with closed sources. Disadvantage of ^{192}Ir is the wide photon spectrum. The spectrum is not ideal for imaging, since the energy of the peak with highest intensity is far below the highest energy (Figure 5.5). When the energy scale of the detector is set to measure the peak with highest intensity, photons with high initial energy can still be detected even after several interactions with the medium. This increases the amount of scattered photons in observations and therefore blurs the image.

Another disadvantage of the Ir sources is the linearity. The linear sources are suitable for resolving of the characteristics of the imaging system, but the real-life distributions are never point-like. If the distribution is known to be point-like, it could be taken into account when choosing the reconstruction method. With appropriate priors the characteristics of the point-like distribution could be taken into account and results would probably be better. However, even if the use of e.g. L_1 prior in reconstruction would produce accurate reconstructions in phantom measurements, it could not be used with real-life data and therefore the performance characteristics of the 6P-SPECT would be overestimated.

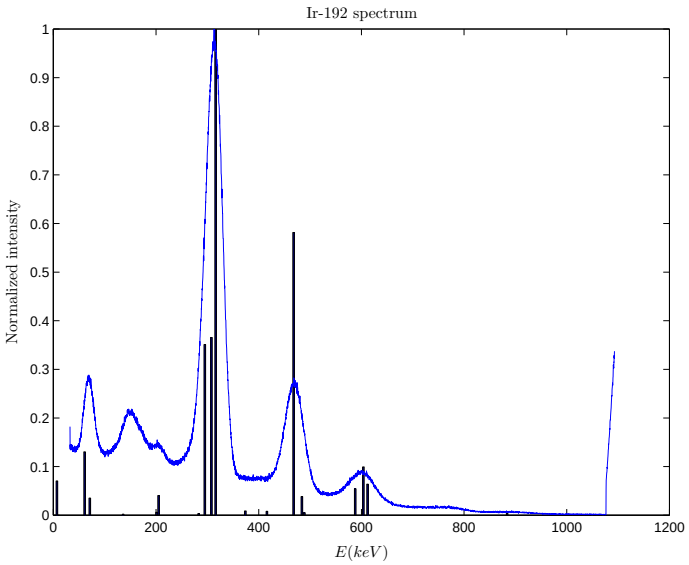

Figure 5.5: Normalized ^{192}Ir photon spectrum. The number of emitted photons as a function of photon energy $E(keV)$. Tabulated values obtained from [8] are presented as histogram and measured with a continuous line.

5.1.3 Detectors

To achieve better sensitivity and reduce the effect of scatter in projection data, single scintillation crystal was used as the radiation detector. Since each of the collimator holes was measured separately the count rates were low enough to be detected.

The use of scintillation crystal makes it possible to eliminate fraction of scattered photons by an *energy window*. The use of energy window reduces the effect of scatter but does not completely eliminate it.

Measurements were conducted by scanning the detector bank hole-by-hole with fixed measurement time per hole. Since the scintillation crystal had a diameter of 5.8 cm, shielding pieces (see Figures 5.4 and 5.3) were constructed to eliminate the radiation from other collimator holes and past the collimator. Shields were made at the *Department of Oncology* in *Kuopio University Hospital* from alloy used in external beam radiotherapy blocking filters.

Disadvantage of the scanning method is the required time. Shorter measurement time could be achieved with more sophisticated detector system. Other possibilities for photon detection are, for example, single scintillation crystal with photomultipliers, or one diode for each collimator hole. With efficient one-row collimator used in 6P-SPECT the count rates in one projection are low enough to be detected by single crystal. The development of the detectors is, however, out of the scope of this thesis.

The used devices were *Nuclear Enterprises Scintillation Counter 663 C* scintillation crystal and *Nuclear Enterprises Scaler-Ratemeter SR3* one-channel analyzer. The settings for *SR3*-analyzer for ^{192}Ir measurements were same in all measurements.

Energy window

Before the actual measurements the difference between 5 and 10% energy windows was verified with one-projection measurements. One line source at the center of the imaging area was used. Measurements were done both in air and in water phantom with diameter of 25 cm. When energy window was lowered to 5% the total number of counts at the maximum point of the projection was reduced to approximately half compared to the measurements with 10% energy window. At the same the "tails" of the projection peak were lowered and the peak became sharper. (see Figure 5.6). We chose to use the smaller (5%) energy window in all measurements since scatter is not considered in observation model.

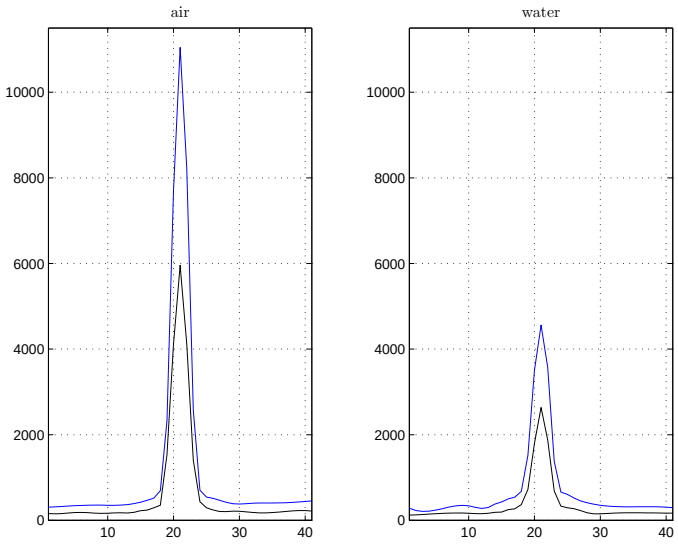

Figure 5.6: Single projections measured in air and in water phantom for selection of energy window. In both figures the projection measured with 10% energy window is drawn with blue and 5% window with black.

5.1.4 Phantoms

Two phantoms were used in the measurements. First phantom consisted of ^{192}Ir wire sources located in water tank whose diameter was 25 cm and height 5 cm. Placements of the sources in phantom was symmetrical with respect to the center of the water tank which was also at the center of rotation. Length of the sources was 3 cm and they were placed in vertical direction. Center of the sources was at the same plane that the center of the collimator holes. This way the assumptions of $2\frac{1}{2}$D-model were satisfied.

The second phantom was a square Lucite block with ^{192}Ir wire sources. This phantom was used for dose measurements with TLD-pellets (see the following Section). The performed experiments are summarized below.

- **Arrangement 1:** Water phantom. One source with total activity of 2.51 mCi located 5 cm from the center of rotation straight toward one of the projections.
- **Arrangement 2:** Water phantom. Two sources with activities of 2.16 and 1.44 mCi (3/2) located 2.5 cm from the center of rotation. Sources were placed approximately in the middle between projection angles, i.e. the line connecting the sources intersects the collimator holes in 30° angle.
- **Arrangement 3:** Same as arrangement 2 but sources were located 5 cm from the center of rotation.
- **Arrangement 4:** Lucite phantom with a single ^{192}Ir source located 3 cm from the center of the phantom with the activity of 1.24 mCi. 22 TLDs were placed inside the phantom to measure dose profiles. Two 1 cm thick water-equivalent plates were placed above and under the Lucite phantom to achieve full scatter conditions in vertical direction.
- **Arrangement 5:** Same as arrangement 4 but with two sources at 3 cm from the center of the phantom symmetrically. Activities of the sources were 1.24 and 0.83 mCi.

The settings of the one-channel analyzer were the same in all measurements. Used energy window was 5% and measurement time per collimator hole was 60 seconds. The energy scale was set to measure the peak with highest intensity in Figure 5.5, that is near 360 keV. This, of course, adds scatter to the projection data from the photons with higher energies but all other peak energies have too low intensity to be measured in reasonable time. With these phantoms and settings the maximum number of detected counts in projections altered between 2500 and 4500 counts per minute. The background, that is, the number of detected pulses at the most distant projection pixels was around 200 pulses per minute in all measurements.

Phantom for dose measurements

When the activity distribution is reconstructed, it can be used to calculate dose distribution in the phantom. To test the algorithm presented in Chapter 4, a Lucite phantom was constructed. TLDs were placed inside the three-layer phantom to measure dose profiles in two directions. Phantom had also a hole with a diameter of 2.8 cm to simulate inhomogeneity in tissues. Width of the square phantom was 16.0 cm and height 4.5 cm (see Figures 5.7 and 5.8). Ir-sources were placed 3 cm from the center of the phantom symmetrically. In the middle layer there were 26 holes for TLDs for dose profile measurements. Dose profiles were measured in two directions and the distance between TLDs was 1.5 mm. Dose was also measured at several points behind the air gap (Figure 5.8). During measurements two one centimeter thick water-equivalent plastic plates were placed above and under the Lucite phantom to achieve full scatter conditions also in vertical direction.

Lithium borate TLDs were used in dose measurement. Before each measurement the TLDs were heated to 300°C and kept in this temperature for an hour. The heating clears the absorbed radiation energy from the pellet and zeros the TLDs. TLDs were exposed inside the phantom for over 40 hours. Measurement time for dose profile was long because the activity of the iridium sources was low compared to the normally used wires. After that the exposure pellets were read

with *Alnor Dosacus* TLD-reader. Individual calibration of the pellets was performed by exposing them to a dose of 1 Gy by an clinical accelerator and measuring the response with TLD-reader. TLDs have linear response in large variation of dose and calibration was done using only one measurement.

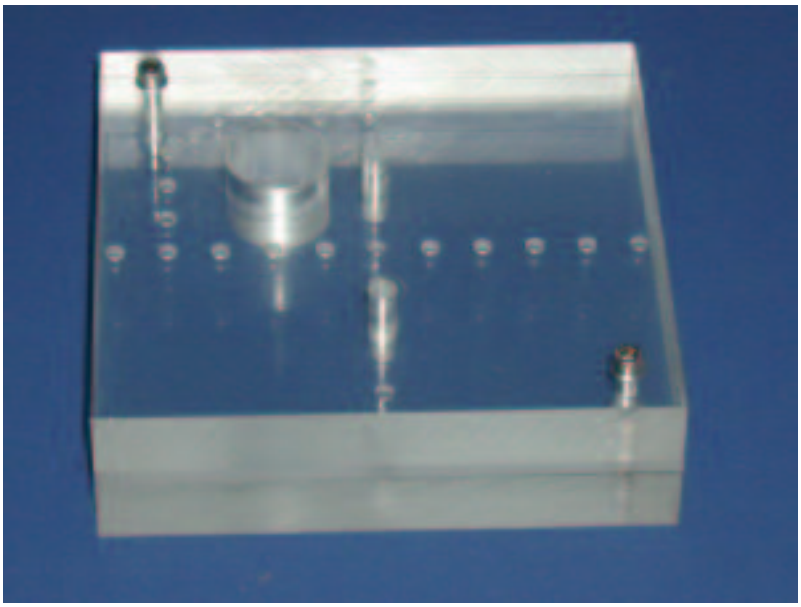

Figure 5.7: Lucite phantom. Width of the square phantom is 16.0 cm and height 4.5 cm.

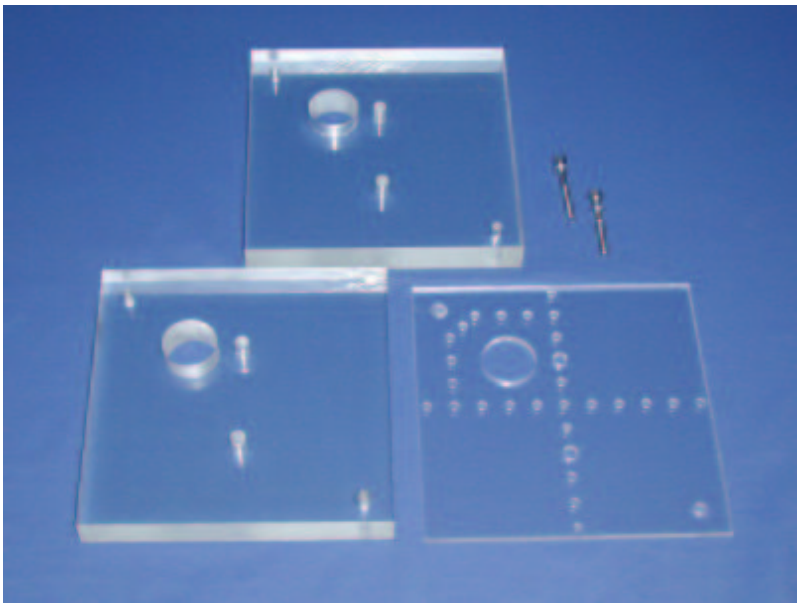

Figure 5.8: Phantom consists of three layers, two 2 cm thick layers at the top and the bottom and 0.5 cm, thick layer in the middle. TLDs were placed in the middle layer.

5.2 Numerical simulation

For this simulation we form an simulated neck phantom of 80 × 80 pixels. Phantom consists of three active areas, two presenting thyroids with high activity and the rest is tissue with background activity (10 % of the activity in thyroids). Also the attenuation map including soft tissue, spine and bronchus is constructed. The activity per pixel is set to 10 kBq at the thyroid area and 1 kBq in soft tissue area, furthermore, the linear attenuation coefficients are chosen as for ^{131}I: $\mu_w = 0.011$ mm^{-1} for soft tissues and $\mu_b = 0.1247$ mm^{-1} for bone (spine).

The projections are calculated using attenuation and collimator corrected $2\frac{1}{2}$D model, (Chapter 2), and using the parameters of 6P-SPECT. In the calculation of the observations the correct attenuation map is used and the resolution of the simulated distributions is 80×80. The reconstructions are calculated with image resolution of 64×64 to avoid an "inverse crime". If the exactly same model is used to calculate both the observations and the inverse problem, the characteristics of the applied model may result in too accurate reconstructions, which is known as a inverse crime. By using more dense grid in calculation of the observations inverse crime can be avoided.

The number of emissions from a point source with activity A is a Poisson-distributed random variable. Therefore the calculated projections are replaced with Poisson distributed random projections with the original projections as the expected values. Also Gaussian noise is added to the randomized projections. The expected value of added noise is 10 % of the mean of the projection values.

Activity distribution is reconstructed using several different methods:

- $2\frac{1}{2}$D model with correct attenuation map.
- $2\frac{1}{2}$D model with homogeneous attenuation map (area of soft tissue)
- $2\frac{1}{2}$D model without attenuation correction
- 2D model with correct attenuation map

Reconstructed images are shown in Figure 5.9. In Figure 5.10 are represented the profiles from three different segments of the reconstructed images. All results from this phantom study are normalized with respect to the simulated activity.

From the profiles presented in Figure 5.10 can be seen that the reconstruction with attenuation correction (correct or homogeneous) give more reliable results than reconstruction without attenuation correction. The peak values of reconstruction with correct attenuation map are slightly better than with reconstruction with homogeneous attenuation map. Homogeneous attenuation map estimates better the lack of background activity in the two nonactive areas. This, however, results also a loss of activity in central area in reconstruction. Without attenuation correction the background activity will not be smooth and underestimation of the hot spots is done.

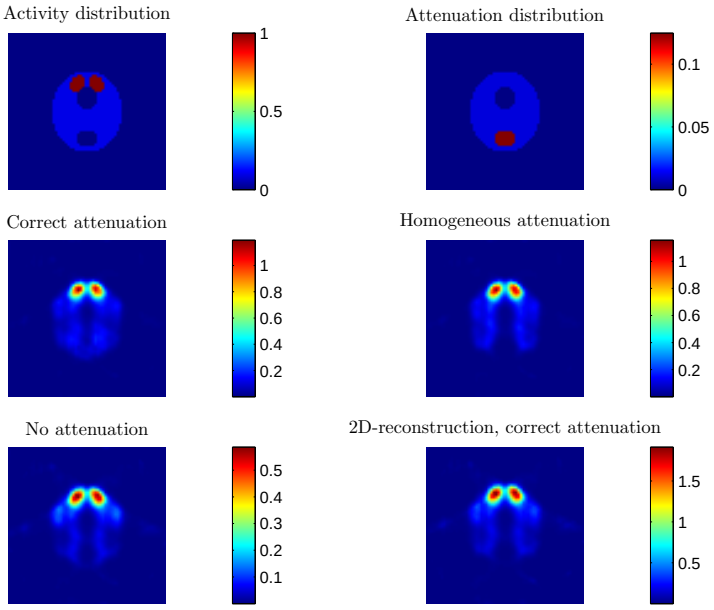

Figure 5.9: Reconstructions from simulation. On the first row are presented the simulated activity and attenuation distributions. On the second row there are presented reconstructions with $2\frac{1}{2}$D model, first with correct attenuation map and then with homogeneous attenuation map. On the last row are shown reconstructions with $2\frac{1}{2}$D model without attenuation correction and 2D model with correct attenuation map. All figures are normalized with respect to the simulated activity distibution.

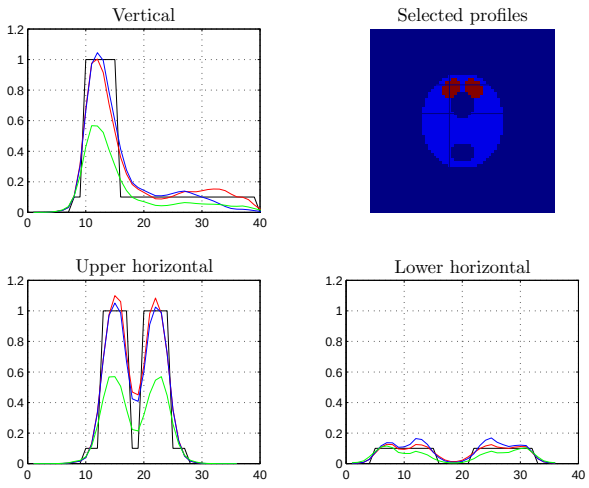

Figure 5.10: Profiles from the reconstructed images of the simulation study (Figure 5.9). On top right are presented the places of the profiles presented in other plots. Reconstruction with correct attenuation map is presented in red, homogeneous with blue and without attenuation correction with green. Results are normalized with respect to the simulated activity distribution.

5.3 Water phantoms - Reconstruction of the activity distribution

5.3.1 Reconstruction methods

In this Section are shown the reconstructions of real measurement data using different reconstruction methods. This is done mainly to demonstrate the power of ML-estimate in reconstruction of activity distribution from limited number of projections.

The used measurement data was acquired with measurement arrangement 3 (Section 5.1.4). Projections were acquired to six constantly spaced angles as in Figure 5.2.

Five different reconstructions were made. The used observation model was collimator and attenuation corrected $2\frac{1}{2}$D-model. First maximum likelihood estimate was calculated using the normal observation model and then with the ROI-constrained model. Number of iterations in ML-EM algorithm was 20 in both cases. Then a minimum norm estimate was calculated using the normal observation model. The ROI-constrained model can not be used when minimum norm estimate is calculated. It produces several positive and negative peaks, that do not correspond to the real activity distribution. Filtered back projection was calculated using a *Hamming*-smoothing window. The cut-off frequency of the ramp filter was set to 1, that is, no modifications to the filter was done. Spline-interpolation was used in back-projection. Finally a standard Tikhonov-regularized estimate was calculated with regularization parameter $\alpha = 10^{-3}$.

Reconstructed images are presented in Figure 5.11. The superiority of ML-estimate is clear, in both normal and ROI-constrained models. The minimum norm estimate is strongly affected by the edge effects in observation model described in Section 2.3.1. It also produces negative artifacts. Filtered back projection practically only back-projects the projections with no assumptions of imaging system or attenuation. Therefore the traces of projections are clearly visible and in intersection points of projection lines produce hot spots. FBP-algorithm also produces negative artifacts. The scaling of the reconstructed image is wrong due the algorithm that was used. Standard Tikhonov regularization does not produce satisfying reconstructions either. Use of more sophisticated priors, for example non-negativity constrain, could improve the reconstruction. This, however, leads to a nonlinear problem and iterative methods are required.

In the following phantom studies all reconstructions are calculated using ML-EM algorithm with 20 iterations.

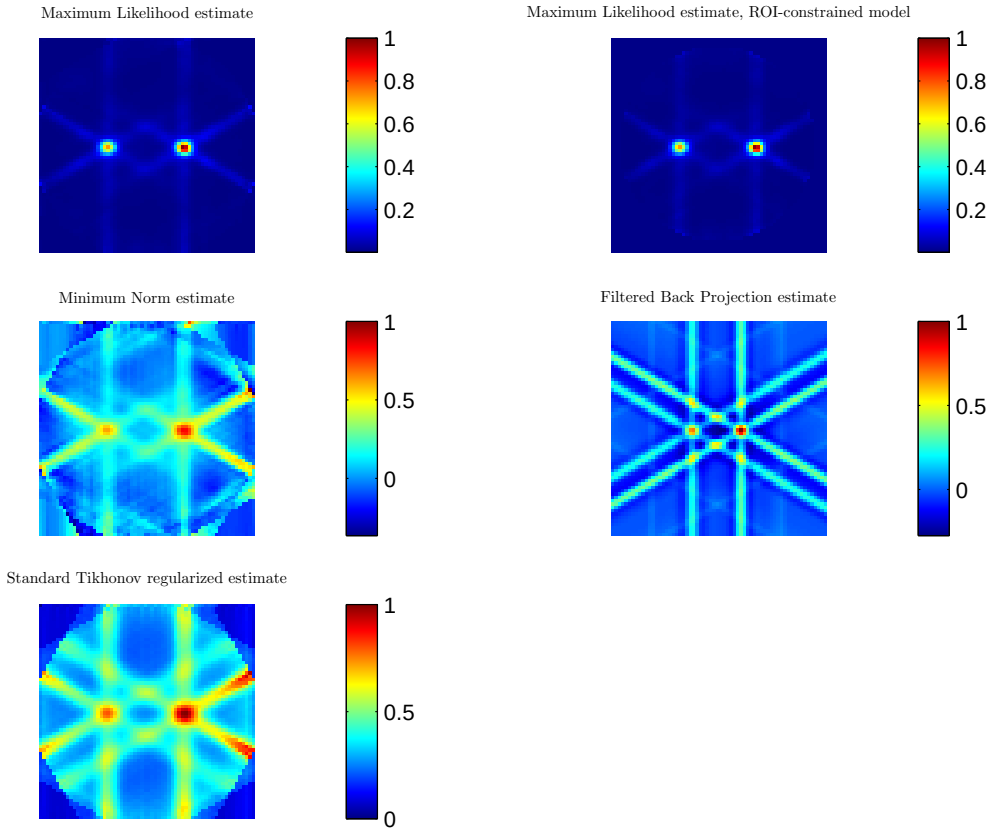

Figure 5.11: Reconstructions from measurement data of phantom 1 using different methods. Calculated estimates are Maximum Likelihood for normal and ROI-constrained model, Minimum Norm, Filtered Back Projection and Standard Tikhonov estimate.

5.3.2 Linearity of image area

The response of imaging system with respect to source position was tested by measurement arrangements 2 and 3. Projections were measured to constantly spaced angles, using both 5 and 6 measurement angles.

We determined profiles over the reconstructed point sources to view the relative activity in pixels. The values from all measurements were satisfying, reconstruction from six projections is slightly better than with the same phantom but with 5 projections. When sources are near each other, the image blurs and relative doses are not as reliable as when sources are at longer distance.

TABLE 5.2: Relative activity of the smaller source and difference to real value in percentages in two-source phantom measurements with different phantoms. The true activity of the smaller source is 2/3 of the higher activity.

	Relative activity	difference(%)
Phantom 2, six angles	0.61	8.7
Phantom 3, six angles	0.67	0.8
Phantom 3, five angles	0.63	5.2

5.3.3 System resolution

In this study we used arrangements 1, 2 and 3. Projections were measured as in Section 5.3.2. Resolution was determined as full width half maximum - values (FWHM). Values were determined from reconstructed images by searching the highest activity and interpolating the FWHM-values to both x and y direction (with two sources the FWHM is determined from point source with larger activity). Resolution was calculated as mean of the x and y FWHM's.

Resolutions obtained from different phantoms are presented in Table 5.3. Reconstructed activity distributions are presented in Figure 5.12.

From images in Figure 5.12 it is easy to see that when the two point sources are near each other, the resolution reduces. Collimator blurring causes also distortion in image since in some angles the both of the sources are visible for a single collimator hole. Collimator effect is however is taken into account in the modeling of the problem. Therefore the image degradation is mostly due to the scatter, that is not modeled in the observation model.

TABLE 5.3: FWHM's in different phantoms.

	spacing	FWHM (mm)
Phantom 1	-	3.2
Phantom 2	5 cm	4.1
Phantom 3, six angles	10 cm	3.3
Phantom 3, five angles	10 cm	3.4

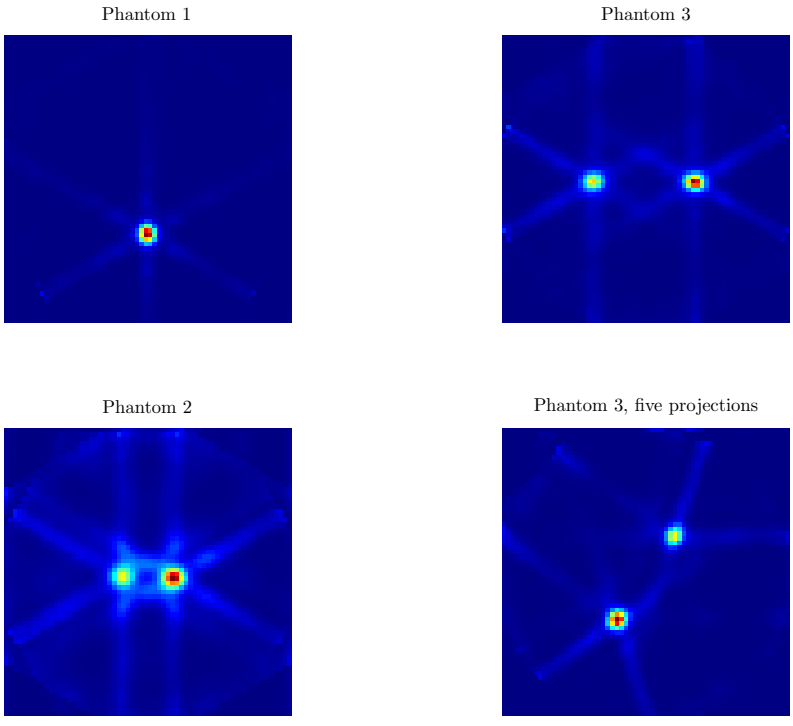

Figure 5.12: Reconstructed activity distributions from phantom measurements. At top left one point source phantom and at right two point sources with distance of 10 cm. At bottom left two point sources with distance of 5 cm and at right same phantom as above but reconstructed from 5 projections.

5.4 Lucite phantom - Dose calculation

To verify the dose calculation methods given in Chapter 4, a Lucite phantom (Figures 5.7 and 5.8) was used for simultaneous measurement of projections and dose distribution. Again ^{192}Ir wire sources were used in measurements. For linear attenuation coefficient and kerma-to-dose conversion factor k we used values for 400 keV peak energy photon radiation [19] . The used values for physical properties of Lucite were:

- $\rho = 1180$ kg/m^2
- $\mu/\rho = 0.1031$ cm^2/g (for 400 keV photons)
- k or $(\frac{\mu}{\rho})^{\text{med}}_{\text{air}} = 1.065$ (for 400 keV photons)

For $SDCC(r)$ curve we used parameters q_i determined for ^{131}I (Table 4.3). Although the spectrum of iodine and iridium differ (see Figures 5.5 and 5.13), the highest intensity of emitted photon is in both near 350 keV and the approximation can be done. For scatter correction we used Meisberger's polynomial for ^{192}Ir in water. Coefficients for Meisberger's scatter polynomial are given in Table 4.2.

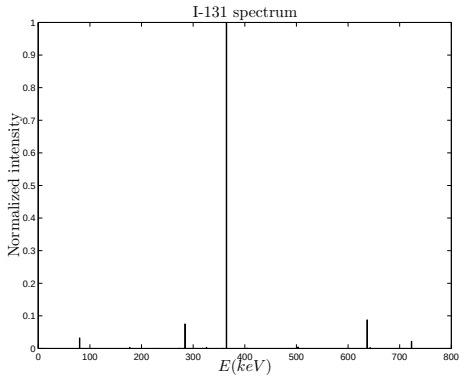

Figure 5.13: Normalized ^{131}I spectrum.

Two different measurements were conducted. First measurement was done using single wire source and the second with two sources. Projections were measured to six equally spaced angles. Dose calculation was based on collimator and attenuation corrected ML-estimate with 20 iterations. Dose was calibrated by single surface measurement according to Eq. (4.9). To speed up the dose calculation 10% threshold of activity was used. This means that only pixels with activity over 10% of the maximum value in the image plane were included in the dose calculation.

In the dose measurements the exposure times for TLDs were too short. The smallest doses were only few cGy and since the calibration was done using reference dose of 1 Gy, there can be some inaccuracy in the measured doses.

5.4.1 Single source

The measured and calculated doses are presented in Table 5.4 and in Figures 5.14 and 5.15. It is easy to find that at the measurement points closest to the source the dose is overestimated. However, at the more distant measurement points the calculated dose is quite accurate. Even the effect of inhomogeneity is modeled in dose calculation, the dose behind the hole is also overestimated. Since the dose calculation model does not concern the reduced scatter conditions in the area of the inhomogeneity (hole), the overestimation is an expected result in the neighborhood of the inhomogeneity.

The overestimation of the near-field doses is caused by the limited resolution of 6P-SPECT. The cross-section of the used iridium source is actually less than one mm^2, however, in the reconstructions the FWHM of the source is more than three millimeters (Section 5.3.3). Since in the

dose calculation each of the pixels is assumed to be individual point source, the summation over the active area of the image produces inaccurate estimates in the near-field of the actual source. We choose not to put great effort into solving this problem since in the real-life cases of radionuclide therapy the activity distributions are never like in these phantom studies. Furthermore, the dose in brachytherapy can be calculated in accurate way by locating the interstitial sources with X-ray imaging and using the dose calculation methods derived for linear sources.

In radionuclide therapy the diffusion and transportation of the active compounds produce smooth distributions and furthermore, there is always some kind of background activity present in the healthy tissues and the effect of limited resolution should not be so remarkable. After all, more phantom studies are required to evaluate the efficiency of the dose calculation in the case of smooth activity distributions. We do not have the possibility to conduct a measurement with open sources for simulating the diffuse distributions of the actual treatments.

5.4.2 Two sources

Measured and calculated doses are presented in Table 5.5 and in Figure 5.17. At the horizontal profile (Figure 5.16) the calculated dose is quite accurate at the distances greater than 3 cm. The spread of point sources in the activity reconstruction affects the dose estimate in the near field and overestimation of the dose is done. Also the measurements behind the air gap show that the dose is overestimated as in the case of single source.

To demonstrate the effect of limited resolution of SPECT in the dose calculation, another dose estimate was calculated. Here we have manipulated the reconstructed activity distribution by selecting only the local maxima of the image, that is, only two pixels in the image area are greater than zero. Results are shown in Table 5.6 and in Figures 5.18 and 5.19. When dose is calculated based on this post-processed activity distribution, the near filed estimate is also quite accurate. Even the results from manipulated activity distribution overcome the ones obtained using plain reconstructions, the method itself is not acceptable. If the activity distribution is known to be point-like, like in this case, the prior information should be included in the reconstruction and the post-processing of the image should not be done. One approach of estimating point-like distributions is the use of so-called L_1 priors [25]. This prior allow few large deviations with small supports in the reconstruction. Since the use of L_1 priors is not reasonable in real cases in radionuclide therapy and the calculation of the estimate will be difficult and time-consuming, we did not use them in this thesis.

TABLE 5.4: Measured and calculated dose and difference between the measured and calculated values in percentages for single source Lucite phantom. The values at horizontal profile are presented from left to right, vertical from top to bottom, excluding the center point. Values around the hole are presented from left to right. The dose measured at the phantom surface was 0.025 Gy (see Figure 5.14).

D(Gy)								
Horizontal			Vertical			Around hole		
Meas.	Calc.	difference (%)	Meas.	Calc.	difference (%)	Meas.	Calc.	difference (%)
0.044	0.046	6.2	0.024	0.025	3.7	0.035	0.036	4.3
0.070	0.071	2.4	0.038	0.037	-3.9	0.026	0.031	21.0
0.111	0.116	4.1	0.095	0.105	10.9	0.018	0.030	59.0
0.183	0.186	1.7	0.704	1.111	57.9	0.022	0.029	31.2
0.222	0.240	8.2	0.735	2.598	253.4	0.021	0.028	30.6
0.192	0.204	6.6	0.237	0.449	89.4	0.025	0.027	7.2
0.124	0.132	6.2	-	-	-	0.022	0.024	10.2
0.078	0.081	3.5	-	-	-	-	-	-
0.048	0.052	8.0	-	-	-	-	-	-

TABLE 5.5: Measured and calculated dose and difference between the measured and calculated values in percentages for two-source Lucite phantom. The values at horizontal profile are presented from left to right, vertical from top to bottom, excluding the center point. Values around the hole are presented from left to right. The dose measured at the phantom surface was 0.044 Gy (see Figure 5.16).

D(Gy)								
Horizontal			Vertical			Around hole		
Meas.	Calc.	difference (%)	Meas.	Calc.	difference (%)	Meas.	Calc.	difference (%)
0.085	0.089	4.8	0.209	0.235	12.4	0.086	0.087	1.6
0.134	0.141	5.2	0.641	1.242	93.7	0.084	0.088	4.0
0.222	0.246	10.5	0.707	1.542	118.1	0.072	0.081	12.4
0.352	0.475	35.1	0.870	2.028	133.1	0.085	0.095	11.9
0.433	0.978	125.8	0.993	2.230	124.6	0.087	0.101	15.6
0.332	0.464	39.7	0.285	0.427	49.8	0.118	0.135	14.6
0.220	0.242	9.6	-	-	-	0.173	0.182	5.4
0.137	0.139	1.7	-	-	-	-	-	-
0.087	0.087	0	-	-	-	-	-	-

TABLE 5.6: Measured and calculated dose and difference between the measured and calculated values in percentages for two-source Lucite phantom. The dose is calculated based on the manipulated reconstruction, that is, only two pixels in the image area are active. The values at horizontal profile are presented from left to right, vertical from top to bottom, excluding the center point. Values around the hole are presented from left to right. The dose measured at the phantom surface was 0.044 Gy (see Figure 5.18)

D(Gy)								
Horizontal			Vertical			Around hole		
Meas.	Calc.	difference (%)	Meas.	Calc.	difference (%)	Meas.	Calc.	difference (%)
0.085	0.090	6.1	0.209	0.191	-8.4	0.086	0.088	2.9
0.134	0.144	7.1	0.641	0.695	8.4	0.084	0.091	7.8
0.222	0.243	9.2	0.707	0.895	26.5	0.072	0.085	17.8
0.352	0.400	12.6	0.870	1.300	49.0	0.085	0.098	15.6
0.433	0.471	8.7	0.993	1.057	6.5	0.087	0.105	20.1
0.332	0.347	4.7	0.285	0.276	-3.2	0.118	0.137	15.6
0.220	0.207	-6.2	-	-	-	0.173	0.167	-3.3
0.137	0.124	-9.4	-	-	-	-	-	-
0.087	0.079	-9.2	-	-	-	-	-	-

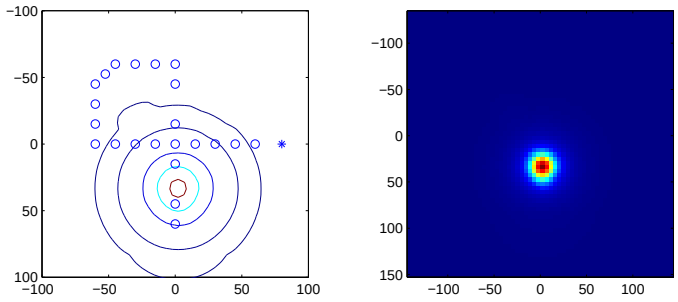

Figure 5.14: Dose distribution in the Lucite phantom with a single source. Dose is calculated based on the raw reconstruction. At left the positions of TLDs are marked with circles and the point of reference surface dose measurement with a star.

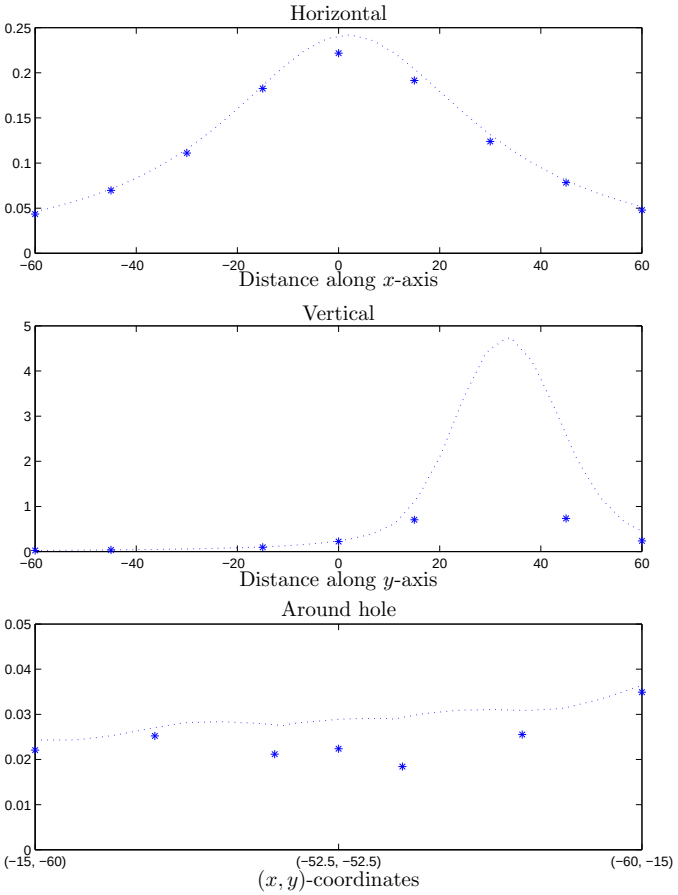

Figure 5.15: Dose profiles for the phantom with a single source based on the raw reconstruction. Measured values are shown with stars and interpolated profiles from the calculated dose distribution with dotted line.

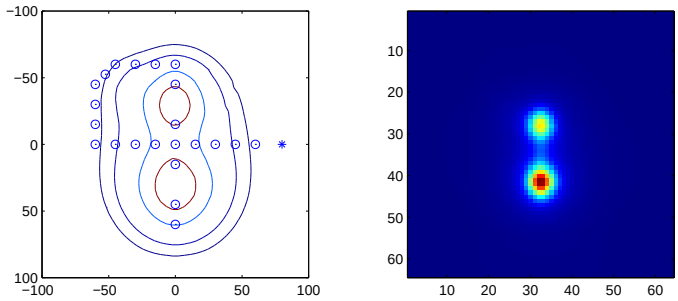

Figure 5.16: Dose distribution in the Lucite phantom with two sources. Dose is calculated based on the raw reconstruction. At left the positions of TLDs are marked with circles and the point of reference surface dose measurement with a star.

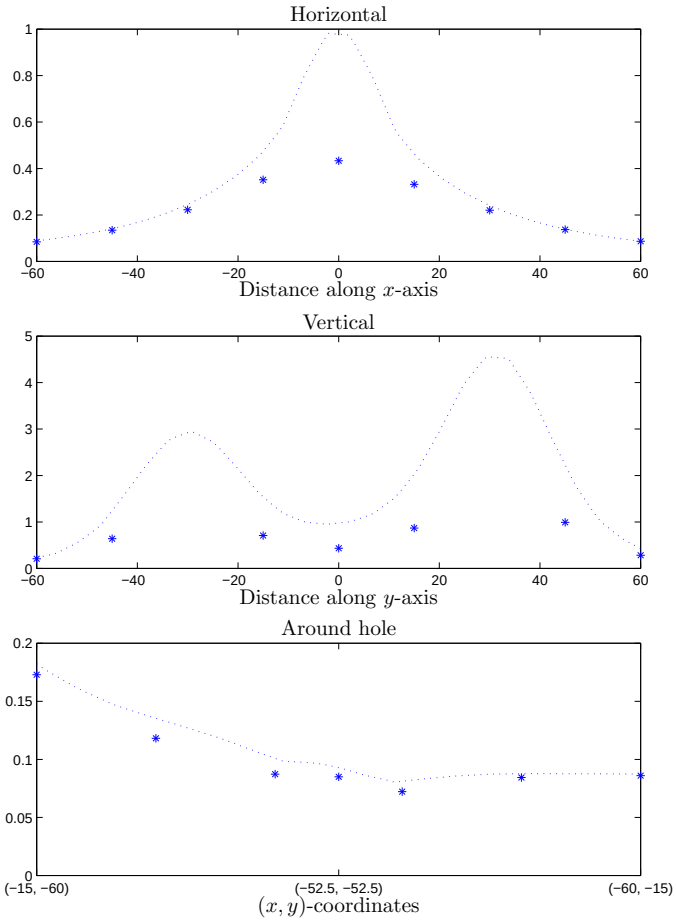

Figure 5.17: Dose profiles for the phantom with two sources based on the raw reconstruction. Measured values are shown with stars and interpolated profiles from the calculated dose distribution with dotted line.

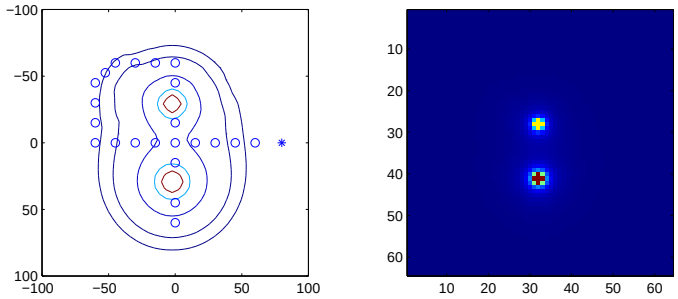

Figure 5.18: Dose distribution in the Lucite phantom with two sources. Dose is calculated based on the manipulated reconstruction. At left the positions of TLDs are marked with circles and the point of reference surface dose measurement with a star.

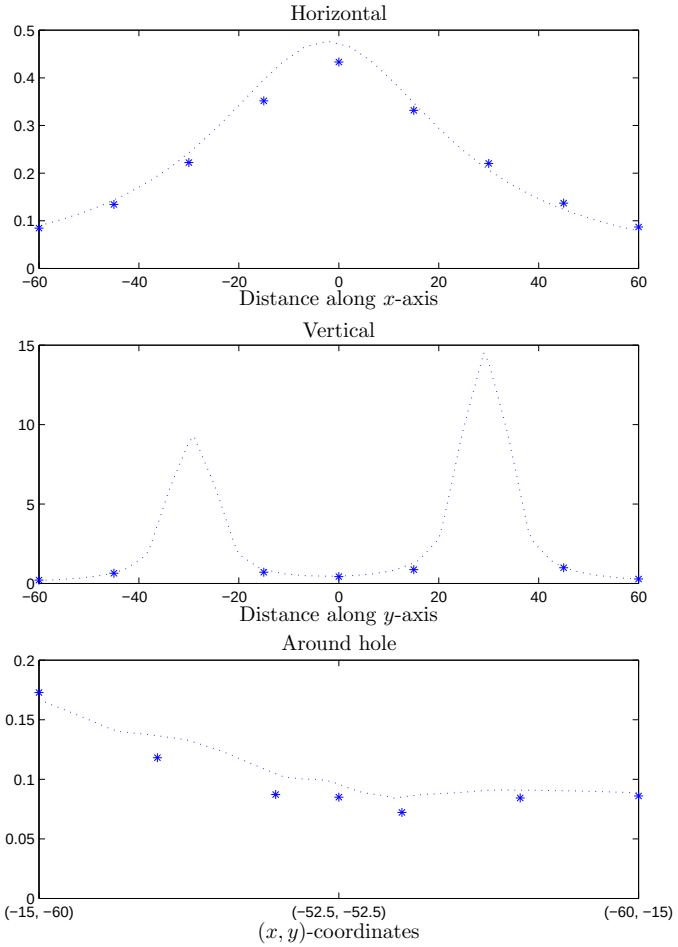

Figure 5.19: Dose profiles in the Lucite phantom with two sources. Dose is calculated based on the manipulated reconstruction. Measured values are presented with stars and interpolated profiles from the calculated dose distribution with dotted line.

Chapter 6

Conclusions and discussion

In this thesis we have considered the reconstruction of the activity distribution of the SPECT images in the case of very limited number of observations, that is, in the case of highly underdeterministic problem. The comparison between the reconstruction methods and different observation models show that the correct modeling and the use of modern reconstruction methods are needed for accurate reconstruction of the activity distribution.

In addition to the image reconstruction in SPECT, dose calculation based on the reconstructed activity distribution is discussed. The statistical inversion is successfully implemented to the on-therapy imaging of radionuclide therapy with an application called 6P-SPECT. The implementation of modern class methods is at the same time necessary and computationally fast in the case of 6P-SPECT due to the low number of projections and the small dimensions of the problem.

A modification of the linear observation model is shown, with purpose to reduce the number of estimation parameters and to regularize the problem. The reduction of parameters is achieved by incorporating the prior information of image areas with zero activity to the observation model in a form of a Region Of Interest - selection.

The calculation of the dose distribution, which is the main goal of on-therapy imaging of the radionuclide therapy, is considered in the Chapter 4. Also a model for correction of inhomogeneous attenuation in dose calculation is given. The imaging system itself does not give quantitative results, however the relative distributions can be calibrated using single surface measurement [28]. The used model for inhomogeneous attenuation is coarse and the different scatter effects of inhomogeneities are not taken into account.

In addition to simulation, series of phantom studies were conducted in order to evaluate the image reconstruction methods and the dose calculation with real measurement data. The superiority of the correct modeling incorporated with statistical inversion in image reconstruction is clearly shown in the reconstructions with real measurement data in the Chapter 5. The measurement time for the projections in the phantom studies was set to one minute. With this selection the maximum number of detected photons in single projection pixels was as low as 5000. Short measurement time was chosen since the manual scanning method, that was used in the projection measurements is time consuming since every projection pixel must be measured separately. The short measurement time produces statistically poor observations. With denser collimation the measurement time would have effect on the sharpness of the projections. However, the resolution of the projections is poor due to the coarse collimator and longer measurement times do not produce significally better results. If the imaging system is developed further, the effect of measurement times and desired number of counts has to be reconcidered.

The dose calculation, verified with simultaneous projection and dose profile measurements, has anyhow yet some shortages. Due to the low number of projections, the "traces" of the linear source towards the projection angles are clearly visible in the activity reconstruction. To reduce the effect errors in activity reconstruction, the activities below 10% of the highest activity were neglected in the dose calculation. Even this manipulation was necessary to estimate the dose distribution from point-like source, in the case of smoother distributions the effect of low resolution is not so

crucial. Although the calibrated dose is quite accurate at the distances greater than 2-3 cm, the estimates near the source differ from the measured values. This is caused by the limited resolution of 6P-SPECT and the use of linear sources in the phantom studies. Further work needs to be done to evaluate the accuracy of the dose estimates in the case of smooth activity distributions, similar to real treatments.

The observation model, that is used in the image reconstruction, still has some deficiencies. The scatter and the septal penetration are the main effects that should be taken into account in the modeling in the future, even the scatter modeling is difficult due to the multiple photo peaks of the therapeutic nuclides. Also the dose calculation should be able to model the altered scatter conditions in the neighborhood of inhomogeneity. Further development has to be done also with the imaging system itself. The detector system should be able to measure the projections in a reasonable time, consequently the scanning method and the TLD detection of the projections can not be considered.

Methods given in this thesis can be used also in fully three-dimensional reconstruction. However, the three-dimensional reconstruction is possible only if the projections are acquired in two dimensions, that is, as a planar image. With the one-row projections of 6P-SPECT the problem is too underdeterministic for three-dimensional reconstruction.

Bibliography

[1] F. H. Attix. *Introduction to Radiological Physics and Radiation Dosimetry.* John Wiley & Sons, 1986.

[2] C. Bai, G. L. Zeng., and G. T. Gullberg. A slice-by-slice blurring model and kernel evaluation using the Klein-Nishina formula for 3D scatter compensation in parallel and converging beam spect. *Physics in Medicine and Biology*, 45(5):1275–1307, 2000.

[3] M. Bardies and M. J. Myers. Computational methods in radionuclide dosimetry. *Physics in Medicine and Biology*, 41:1941–1955, 1996.

[4] F. J. Beekman, C. Kamphuis, M. A. King, P. P. van Rijk, and M. A. Viergever. Improvement of image resolution and quantitative accuracy in clinical single photon emission computed tomography. *Computerized Medical Imaging and Graphics*, 25:135–146, 2001.

[5] M. Bertero and P. Boccacci. *Introduction to Inverse Problems in Imaging.* IOP Publishing Ltd, 1998.

[6] P. Boccacci, P. Bonetto, P. Calvini, and A. R. Formiconi. A simple model for the efficient correction of collimator blur in 3D SPECT imaging. *Inverse Problems*, 15:907–930, 1999.

[7] A. A. Bolster and T. E. Hilditch. The radiation dose to the urinary bladder in radio-iodine therapy. *Physics in Medicine and Biology*, 41(1993-2008), 1996.

[8] J. Borg and D. W. O. Rogers. Monte Carlo calculations of photon spectra in air from ^{192}Ir sources. Technical report, National Research Council, Institute for National Measurement Standards, Ionizing Radiation Standards., Ottawa, Ontario, K1A 06R, Canada, March 1999.

[9] L. Bouwens, R. Van de Walle, J. Nyuts, M. Koole, Y. D'Asseler, S. Vandenberghe, I. Lemahieu, and R. A. Dierckx. Image-correction techniques in SPECT. *Computerized Medical Imaging and Graphics*, 25:117–126, 2001.

[10] S. E. M. Clarke. Radionuclide therapy of the thyroid. *European Journal of Nuclear Medicine*, 18(12):984–991, 1991.

[11] V. Dicken. *Tikhonov-IntraSPECT: Simultaneous Activity and Attenuation Reconstruction in Single Photon Emission Computed Tomography, a Nonlinear Ill-Posed Problem.* PhD thesis, University of Potsdam, November 1997.

[12] G. N. El Fakhri, I. Buvat, M. Pelegrini, H. Benali, and B. Bendriem P. Almeida, A. Todd-Pokropek, and R. Di Paola. Respective roles of scatter, attenuation, depth-dependent collimator response and finite spatial resolution in cardiac single-photon emission computed tomography quantitation: a Monte Carlo study. *European Journal of Nuclear Medicine*, 26(5):437–446, May 1999.

[13] A. R. Formiconi, A. Passeri, M. R. Guelfi, M. Masoni, A. Pupi, U. Meldolesi, P. Malfetti, L. Calori, and A. Guidazzoli. World wide web interface for advanced SPECT reconstruction algorithms implemented on a remote massively parallel computer. *International Journal of Medical Informatics*, 47, 1997.

[14] H. P. Giap, D. J. Macey, J. E. Bayouth, and A. L. Boyer. Validation of a dose-point kernel convolution technique for internal dosimetry. *Physics in Medicine and Biology*, 40:365–381, 1995.

[15] A. J. Green, S. E. Dewhurst, R. H. J. Begent, K. D. Bagshawe, and S. J. Riggs. Accurate quantification of ^{131}I distribution by gamma camera imaging. *European Journal of Nuclear Medicine*, 16:361–365, 1990.

[16] P. J. Green. Bayesian reconstructions from emission tomography data using a modified EM algorithm. *IEEE Transactions on Medical Imaging*, 9(1):84–93, 1990.

[17] C. A. Hoefnagel. Radionuclide therapy revisited. *European Journal of Nuclear Medicine*, 18(6):408–431, 1991.

[18] R. H. Huesman. A new fast algorithm for the evaluation of regions of interest and statistical uncertainty in computed tomography. *Physics in Medicine and Biology*, 29(5):543–552, 1984.

[19] H. E. Johns and J. R. Cunningham. *The Physics of Radiology.* Springfield: Charles C. Thomas, 4$^{\text{th}}$ edition, 1983.

[20] H. Jones, G. Mitra, D. Parkinson, and T. Spinks. A parallel implementation of the maximum likelihood method in positron emission tomography image reconstruction. *Computational Statistics & Data Analysis*, 31:417–439, 1999.

[21] J. Kaipio. Käänteisongelmat. http://venda.uku.fi/∼kaipio/inv/chaps1to5.pdf (29.6.2001) in finnish, 1999. Lecture Notes, University of Kuopio.

[22] A. C. Kak and M. Slaney. *Principles of Computerized Tomographic Imaging.* IEEE Press, 1987.

[23] D. J. Kardmas, E. C. Frey, S. S. Karimi, and B. M. W. Tsui. Fast implementations of reconstruction-based scatter compensation in fully 3D SPECT image reconstruction. *Physics in Medicine and Biology*, 43:857–873, 1998.

[24] P. A. Karjalainen, M. Vauhkonen, and J. P. Kaipio. Time varying reconstruction in single photon emission tomography. Technical Report 4, University Of Kuopio, Department of Applied Physics, http://venda.uku.fi/research/IP/publications/deptrep/rep4.98.pdf (29.6.2001), 1998.

[25] V. Kolehmainen. *Novel Approaches to Image Reconstruction in Diffusion Tomography.* PhD thesis, University of Kuopio, Department of Applied Physics, http://venda.uku.fi/research/IP/publications/deptrep/ville_phd.pdf (29.6.2001), 2001.

[26] K. F. Koral and Y. Dewaraja. I-131 SPECT activity recovery coefficients with implicit or triple-energy-window scatter correction. *Nuclear Instruments and Methods in Physics Research*, A 422:688–692, 1999.

[27] A. Krol, J. E. Bowsher, S. H. Manglos, D. H. Feiglin, M. P. Tornai, and F. D. Thomas. An EM algorithm for estimating SPECT emission and transmission parameters from emission data only. *IEEE Transactions on Medical Imaging*, 20(3):218–232, March 2001.

[28] J. Kulmala. *Absorbed Radiation Dose in Targeted Radionuclide Therapy: A Method Based on Transversal Limited-projection Emission Tomography.* PhD thesis, University of Turku, 1997.

[29] K. Van Laere, M. Koole, I. Lemahieu, and R. Dierckx. Image filtering in single photon emission tomography: Principles and applications. *Computerized Medical Imaging and Graphics*, 25:127–133, March 2001.

[30] T. Lahtinen. Sädehoidon fysiiikka II, 1997. Lecture Notes, University of Kuopio.

[31] T. Lahtinen. Sädehoidon fysiikka I: Sädehoidon dosiometria, 1998. Lecture Notes, University of Kuopio.

[32] K. Lange and R. Carson. EM reconstruction algorithms for emission and transmission tomography. *Journal of Computer Assisted Tomography*, 8(2):306–316, April 1984.

[33] J. Llacer. Theory of imaging with a very limited number of projections. *IEEE Transactions on Nuclear Science*, NS-26(1):596–602, February 1979.

[34] J. Llacer and J. D. Meng. Matrix-based image reconstruction methods for tomography. *IEEE Transactions on Nuclear Science*, NS-32(1):855–864, February 1985.

[35] R. Nath, L. L. Anderson, G. Luxton, K. A. Weaver, J. F. Williamson, and A. S. Meigooni. Dosimetry of interstitial brachytherapy sources: Recommendations of the AAPM radiation therapy committee task group No. 43. *Medical Physics*, 22(2):209–234, February 1995.

[36] Department of Clinical Physiology. Ohje radiojodihoitoa tilaaville yksiköille. Technical report, Kuopio University Hospital, 1988.

[37] Department of Clinical Physiology. Kilpirauhasen liikatoiminnan radiojodihoito. Technical report, Kuopio University Hospital, 1998.

[38] Department of Clinical Physiology. Potilasohje suuriannoksiseen radiojodihoitoon tulevalle potilaalle. Technical report, Kuopio University Hospital, 1998.

[39] R. J. Ott. Imaging technologies for radionuclide dosimetry. *Physics in Medicine and Biology*, 41:1885–1894, 1996.

[40] A. Passeri, A. R. Formiconi, and U. Meldolesi. Physical modelling (geometrical system response, compton scattering and attenuation) in brain SPECT using the conjugate gradients method. *Physics in Medicine and Biology*, 37:1727–1744, 1997.

[41] A. R. De Pierro. A modified expectation maximization algorithm for penalized likelihood estimation in emission tomography. *IEEE Transactions on Medical Imaging*, 14(1):132–137, March 1995.

[42] K. R. Pollard, N. Alden Bice, J. F. Eary, L. D. Durack, and T. K. Lewellen. A method for imaging therapeutic doses of iodine-131 with a clinical gamma camera. *Journal of Nuclear Medicine*, 33(5):771–776, May 1992.

[43] M. H. Selikson, J. Jaggi, D. P. Mozley, L. Lodhi, J. McCue, H. Vu, and R. Forrest. A proposal for minimum detectable compartment in MIRD dosimetry modelling. *Physics in Medicine and Biology*, 42:1605–1617, 1997.

[44] A. O. Seppänen. Correction of collimator blurring and attenuation in single photon emission computed tomography. Master's thesis, University Of Kuopio, Faculty of Natural and Environmental Sciences, Department of Applied Physics, http://venda.uku.fi/∼aoseppan/SPECTthesis.pdf (29.6.2001), 2000.

[45] L. A. Shepp and Y. Vardi. Maximum likelihood reconstruction for emission tomography. *IEEE Transactions on Medical Imaging*, MI-1(2):113–122, October 1982.

[46] R. L. Siddon. Fast calculation of exact radiological path for a three-dimensional CT array. *Medical Physics*, 12:252–255, March 1985.

[47] M. F. Smith, C. E. Floyd, R. J. Jaszczak, and E. R. Coleman. Reconstruction of SPECT images using generalized matrix inverses. *IEEE Transactions on Medical Imaging*, 11(2), June 1992.

[48] M. F. Smith and R. J. Jaszczak. Generalized dual-energy-window scatter compensation in spatially varying media for SPECT. *Physics in Medicine and Biology*, 39:531–546, 1994.

[49] S. Vandenberghe, Y. D. D'Asseler, R. Van de Walle, T. Kauppinen, M. Koole, L. Bouwens, K. Van Laere, I. Lemahieu, and R. A. Dierckx. Iterative reconstruction algorithms in nuclear medicine. *Computerized Medical Imaging and Graphics*, 25:105–111, 2001.

[50] D. F. Yu, J. A. Fessler, and E. P. Ficaro. Maximum-likelihood transmission image reconstruction for overlapping transmission beams. *IEEE Transactions on Medical Imaging*, 19(11):1094–1105, November 2000.

[51] S. Zhang and Y. M. Wang. An approach to positron emission tomography based on penalized cross-entropy minimization. *Signal Processing*, 81:1069–1074, 2001.